

Wideband 2-D Array Design Optimization With Fabrication Constraints for 3-D US Imaging

Emmanuel Roux, *Student Member, IEEE*, Alessandro Ramalli, *Member, IEEE*,
Hervé Liebgott, *Associate Member, IEEE*, Christian Cachard,
Marc C. Robini, and Piero Tortoli, *Senior Member, IEEE*

Abstract—Ultrasound (US) 2-D arrays are of increasing interest due to their electronic steering capability to investigate 3-D regions without requiring any probe movement. These arrays are typically populated by thousands of elements that, ideally, should be individually driven by the companion scanner. Since this is not convenient, the so-called microbeamforming methods, yielding a prebeamforming stage performed in the probe handle by suitable custom integrated circuits, have so far been implemented in a few commercial high-end scanners. A possible approach to implement relatively cheap and efficient 3-D US imaging systems is using 2-D sparse arrays in which a limited number of elements can be coupled to an equal number of independent transmit/receive channels. In order to obtain US beams with adequate characteristics all over the investigated volume, the layout of such arrays must be carefully designed. This paper provides guidelines to design, by using simulated annealing optimization, 2-D sparse arrays capable of fitting specific applications or fabrication/implementation constraints. In particular, an original energy function based on multidepth 3-D analysis of the beam pattern is also exploited. A tutorial example is given, addressed to find the N_e elements that should be activated in a 2-D fully populated array to yield efficient acoustic radiating performance over the entire volume. The proposed method is applied to a 32×32 array centered at 3 MHz to select the 128, 192, and 256 elements that provide the best acoustic performance. It is shown that the 256-element optimized array yields sidelobe levels even lower (by 5.7 dB) than that of the reference 716-element circular and (by 10.3 dB) than that of the reference 1024-element array.

Index Terms—2-D transducers, 3-D ultrasound (US), simulated annealing (SA), sparse array.

I. INTRODUCTION: 2-D ARRAY DESIGNS FOR 3-D ULTRASOUND IMAGING (STATE-OF-THE-ART)

FEW imaging systems can be simultaneously defined as portable, nonionizing, relatively inexpensive, and fully interactive, thanks to real-time operation. All of these features characterize the 2-D ultrasound (2D-US) scanners that are widely used in the clinical environment for the diagnosis of several diseases. Even if highly successful, 2D-US is inherently limited to display 2-D slices of the 3-D reality of organs, thus forcing doctors to mentally reconstruct the observed volume. This lack of volumetric information has motivated many investigations in both academic and industrial research departments [1]–[11]. Three-dimensional real-time US imaging [1] allow accessing arbitrary tissue slices [2], assessing 3-D mechanical properties of tissues [3], [4], measuring 3-D vector blood flow [5], assisting surgery (e.g., for biopsy needle tracking) [6], [7], or high intensity focused US (HIFU) monitoring [8], [9]. In particular, real-time 3-D echocardiography is one of the most challenging US applications [2], [10], [11] because it requires a very high spatiotemporal resolution, i.e., high volume rates while maintaining the precision and robustness in the spatial domain.

Before the development of electronic steering [12], single-element transducers were manually or mechanically translated to create 2-D images. The same trend has taken place in the passage from 2-D to 3-D imaging, which actually started with position-tracked or motorized 1-D arrays that were translated/rotated/tilted to scan a volume. Recently, 3-D imaging was made more feasible by the introduction of 2-D array probes that are able to steer US waves in both the directions (elevation and azimuthal) [1], [10], [13]–[15]. In order to run the probe with the highest flexibility, one channel of the scanner should be continuously connected to one active element, so that each transmission signal, transmit/receive timing, and apodization can be independently controlled to implement specific imaging sequences. Unfortunately, in full 2-D arrays, the need for maintaining the pitch smaller than half the wavelength λ leads to a large number (up to thousands) of small-sized elements. Connecting several thousands of elements in a one-element-to-one-channel (one-to-one) design increases the electronic circuit complexity and makes the connection probe cable unsuitable in the clinical practice. For example, let us assume a 20-mm aperture (e.g., for parasternal cardiac imaging) and a central frequency

Manuscript received July 21, 2016; accepted September 29, 2016. Date of publication October 3, 2016; date of current version January 11, 2017. This work was supported in part by la Région Rhône-Alpes under Grant CMIRA 2014, in part by Université Franco-Italienne under Grant VINCI 2014 and Grant C2-13, in part by the European Union through the ENIAC JU Project DeNeCoR under Grant 324257, and in part by the framework of the LABEX CELYA (ANR-10-LABX-0060) (PALSE mobility Grant) and LABEX PRIMES (ANR-11-LABX-0063) of Université de Lyon, within the Program Investissements d’Avenir (ANR-11-IDEX-0007) operated by the French National Research Agency (ANR). (*Corresponding author: Emmanuel Roux.*)

E. Roux is with the Department of Information Engineering, Università degli Studi di Firenze, 50139 Florence, Italy, also with the CREATIS Laboratory, INSA-Lyon, Université de Lyon, 69007 Lyon, France, and also with Université Claude Bernard Lyon 1, 69100 Villeurbanne, France (e-mail: roux@creatis.univ-lyon1.fr).

A. Ramalli and P. Tortoli are with the Department of Information Engineering, Università degli Studi di Firenze, 50139 Florence, Italy (e-mail: alessandro.ramalli@unifi.it; piero.tortoli@unifi.it).

H. Liebgott, C. Cachard, and M. C. Robini are with the CREATIS Laboratory, INSA-Lyon, Université de Lyon, 69007 Lyon, France, and also with Université Claude Bernard Lyon 1, 69100 Villeurbanne, France (e-mail: liebgott@creatis.univ-lyon1.fr; cachard@creatis.univ-lyon1.fr; robini@creatis.insa-lyon.fr).

This paper has supplementary downloadable material available at <http://ieeexplore.ieee.org>, provided by the authors. This includes three videos illustrating the individual optimization runs of opti128, opti192, opti256, and a readme file. This material is 19 MB in size.

Digital Object Identifier 10.1109/TUFFC.2016.2614776

of 3 MHz. The $513 \mu\text{m}$ ($\lambda/2$) pitch condition (for a speed of sound = 1540 m/s) leads to a $40 \times 40 = 1600$ element array. A possible one-to-one design would also be very demanding in terms of the data transfer rate (1600 elements produce ≈ 1500 Gb/s with 12-b Analog to Digital Converters sampling at 80 MHz), data storing capability (almost 2 TB for each second of acquisition), and computational load (a volume of 128×128 lines, each of 2048 samples, requires 54 G multiply-and-accumulate operations with delay-and-sum reconstruction).

An elegant solution to reduce the cable size and the amount of data to be transferred to and processed by the scanner is represented by the microbeamforming technique [16]–[19]. It allows maintaining thousands of active elements while sending only a reduced number of signals through the probe cable. This is possible thanks to the implementation of a first beamforming step in the probe handle, which delays and sums the signals related to a group of elements (called subaperture). This allows the scanner to control a reduced number of channels but involves the development of expensive application-specific integrated circuits and limits the flexibility in the image reconstruction process. Row-column addressing [13], [14], [20], [21] and channel multiplexing techniques [22], [23] are also promising techniques, but they do not allow continuously running the full array during transmission and reception, as only part of the elements can be connected to the frontend of the scanner at each time.

A more direct solution is to drastically reduce the number of active elements that need to be controlled by the scanner, according to the sparse array methodology [24]. The active elements configuration emerging out of this reduction must, of course, fit the desired imaging features in terms of the resolution and contrast over the entire field of view (FOV). These features are directly bound by the 2-D array beam pattern (BP), whose main lobe (ML) width [full-width at half-maximum (FWHM) at -6 dB], sidelobe level (SLL), and grating lobe level (GLL) affect the 2-D image quality. In the literature, two main approaches have been investigated to find the smartest “sparse” configuration of active elements, which can be defined as deterministic [25]–[32] and nondeterministic [33]–[42], respectively.

Deterministic sparse array designs include conformal arrays [26], regular and radially periodic arrays [28], [29], or Mills cross arrays [31], which can be quickly defined with small computational effort and immediately tested through simulations, as the layout geometry is known in advance. As drawbacks, there is limited design flexibility, and their performance, in terms of SLL/GLL, depends on the use of one set of elements in transmission (TX) and another one in reception (RX), addressed to cancel the grating lobes in the pulse-echo (two-way) BP. If multiplexing cannot be adopted, the total number of elements in TX and RX is limited by the number of scanner channels. Using all of the available channels to activate the same group of elements in both TX and RX maximizes the active surface, which helps in compensating for the lack of sensitivity often attributed to sparse arrays. Recently, the use of special spiral array configurations has been proposed [25], [27], and the related simulations show promising results.

In nondeterministic random sparse arrays, a number of configurations, each obtained by randomly choosing part of the elements of the fully populated 2-D-array, are initially defined. Among them, the configuration yielding the best performance (e.g., in terms of GLL) is selected. With this approach, the number of explored configurations is typically limited [28], [30], [32] and it is not possible to ensure that the best achievable performance is actually obtained. This lack of robustness comes from the fact that each random array is generated independently of the previous tested configurations.

Nondeterministic approaches based on stochastic optimization take advantage from previous trials to iteratively search for the “optimum” configuration. As searching for an optimal configuration among all possible sparse arrays is a very large-scale combinatorial optimization problem, simulated annealing (SA) [24], [33]–[38], [40] is better suited than genetic algorithms [24], [39], [41], [42]. Indeed, the main difficulty in solving a large-scale optimization problem using a genetic algorithm is to manage a large population of candidate solutions, which is expensive in terms of both computation time and memory requirements; besides, genetic algorithms have other drawbacks: they usually converge prematurely and have poor hill-climbing capability (see [43], [44]). For the best performance, the cost functions to be optimized by stochastic methods should be based on the BP features, which is often unpractical since computing a realistic BP for each configuration is time-consuming. In order to reduce the computational load, the majority of stochastic 2-D array design methods [24], [34]–[36], [38]–[42] approximate the BP by a narrowband BP in the far-field. The far-field approximation implies that each active element is reduced to a pointwise source defined by its center and weight (the element size and orientation are not taken into account). The narrowband BP, also known as the continuous wave response, assumes that the transmitted signal is a monochromatic wave at the central frequency of the array (no realistic excitation signal and impulse response are considered). To our knowledge, the only two exceptions are [33] and [37], where stochastic optimization is performed using a wideband two-way point spread function simulation. In addition, layout symmetry is usually enforced to further reduce the computational load and the number of possible configurations [33], [37].

A further distinction between on-grid [29], [33], [36], [38] and out-of-grid [25], [34], [45]–[49] sparse arrays can be made. The former have all of the elements aligned along rows and columns, while in the latter ones the elements do not have any position restriction (except that they cannot overlap). The additional degrees of freedom achieved in this case permit to increase the obtainable acoustic performance [25], [34]. Indeed, out-of-grid designs present the advantage of reducing the GLL even when the interelement distance is greater than $\lambda/2$, thanks to a nonperiodical spatial sampling. Releasing the spatial sampling condition also enables the use of wider elements and compensates for the sparse array sensitivity lack by increasing the active surface of the aperture. However, increasing the element size can potentially limit the FOV: the wider the elements the weaker their steering

capability. However, manufacturing out-of-grid arrays imposes additional requirements on the fabrication process, which could require laser machining technique if piezoelectric or Capacitive Micromachined Ultrasonic Transducers (CMUT) technology is involved [50]. The CMUT fabrication process is very close to that of integrated circuits and, as such, is extremely flexible but, at the same time, very expensive unless thousands of identical probes are fabricated.

This paper provides the guidelines for the layout design of nondeterministic 2-D sparse arrays based on stochastic optimization (SA). The acoustic performance is evaluated by means of wideband and multidepth, fast, and realistic BP simulations repeated at each optimization step [47], [48]. The introduction of multidepth cost functions [48] provides better control of the BP behavior in the volume, which is a step toward 3-D BP optimization. The high BP computation speed allows optimizing the out-of-grid element positions without any BP precalculation nor any *a priori* layout symmetry condition. New degrees of freedom (element size and orientation, impulse response, and excitation signal) can be explored while specific geometrical constraints imposed by the application (e.g., positioning/orientation on a convex surface for HIFU transducers) or the fabrication process (e.g., definition of a suitable spacing between elements to let the circuit lines go through the footprint) can be introduced. An important practical aspect of the proposed method is that the final number of active elements can be fixed in advance. This can be relevant for instance to have a final number of elements equal to the number of available independent channels on a scanner. The finite time convergence properties of the SA algorithm [51]–[54] also allows setting the number of iterations in advance. The required time to perform an optimization process can thus be better controlled.

The proposed method can lead to both on-grid and out-of-grid sparse array designs. Although out-of-grid arrays have promising performance, as discussed above, only a few prototype samples have so far been manufactured. On the other hand, on-grid matrix array probes are already commercially available [22], [55], [56] and their production is expected to increase. For this reason, it looks valuable to illustrate the proposed method by the design of “optimal” sparse array probes whose elements are selected from an on-grid array. SA is used here to find the smartest combination of a given number N_e of elements (the same for both TX and RX to maximize the array sensitivity) in an $N_x N_y$ 2-D gridded array that produces the best possible acoustic performance. The number of active elements $N_e \ll N_x N_y$ would ideally be equal to the number of channels available on the scanner to avoid previously mentioned limitations in the acquisition sequence flexibility and to potentially enable the obtained 2-D array probes’ compatibility with currently available scanners.

This paper is organized as follows. The general optimization method is introduced in Section II. The application to finding the best N_e -combination of active elements in an $N_x N_y$ 2-D array is described in Section III. The results of sparse array designs with $N_e = \{128, 192, 256\}$ elements selected out of a $32 \times 32 = 1024$ element array are presented in Section IV.

Finally, the optimization tool and the results are discussed in Section V.

II. SPARSE ARRAY OPTIMIZATION

A. General 2-D Sparse Array Optimization Model

An optimal 2-D sparse array S_{opti} is searched by minimizing an energy function U over a large (but finite) state space of 2-D sparse arrays Ω . The optimization is performed by a Metropolis-type SA algorithm [51]–[54] that explores Ω iteratively by means of a communication mechanism Θ specifying the possible state transitions. The key feature of SA is that a cooling sequence controls the acceptance probability of the uphill transitions in the Markov chain of the explored solutions. The state-space Ω of 2-D sparse arrays is presented in Section II-A1, the communication mechanism Θ is introduced in Section II-A2, and the energy function U is defined in Section II-A3. The SA optimization workflow is described in Section II-B.

1) *General State Space*: From a general point of view, a 2-D sparse array consists of a reduced number of elements N_e compared with a full array of same aperture size. A general state space of 2-D sparse arrays with N_e elements is of the form

$$\{S = (\mathbf{e}_1, \dots, \mathbf{e}_{N_e}) \in E_1 \times \dots \times E_{N_e} | A_i \cap A_j = \emptyset, \text{ for all } i, j \in [1 \dots N_e] \text{ such that } i \neq j\} \quad (1)$$

where E_k and A_k are, respectively, the set of properties and the spatial region occupied by the k th element \mathbf{e}_k . In other words, a sparse array S is a collection of N_e nonoverlapping elements, each of which is represented by a vector in some space E_k . The spaces E_k can differ from each other, meaning that the elements in a sparse array S can have different types or geometries as long as they do not overlap. However, for computational complexity reasons, we cannot optimize the full set of parameters describing each element. For example, a rectangular element can be described by a vector

$$\mathbf{e}_k = \begin{bmatrix} (x_k, y_k, z_k) \\ (\theta_k, \phi_k) \\ (a_k, b_k) \\ w_k \\ \text{Imp}_k \\ \text{Exc}_k \\ \tau_k \end{bmatrix} \in E_k, \quad (2)$$

where (x_k, y_k, z_k) are the 3-D Cartesian coordinates of the element center, (θ_k, ϕ_k) are the spherical orientation coordinates of the normal vector to the element surface (see Fig. 1 for angle convention), (a_k, b_k) are the element sizes along the x - and y -axes when $(\theta_k, \phi_k) = (0, 0)$, w_k is the element weight for apodization, Imp_k and Exc_k are, respectively, the impulse response and the excitation signal of the element, and τ_k is the transmission delay. In practice, for a given focal point, the individual delays τ_k are determined by the element positions. Moreover, the components of \mathbf{e}_k to be optimized are classically either (x_k, y_k, z_k) or w_k , the other components being fixed and equal for all the elements. So the actual state-space Ω is of

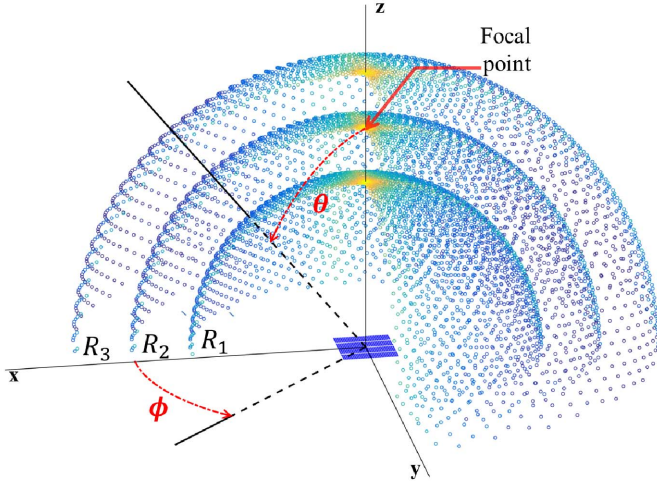


Fig. 1. Example of three hemispheres of PMPs around a 32×32 element 2-D array with (θ, ϕ) the spherical angles convention, where θ is the angle between a point and the z -axis and ϕ is the angle between the projection of this point in the xOy plane and the x -axis.

the form (1), with each E_k replaced by its subset obtained by fixing all the components except the Cartesian coordinates or the weights.

2) *Communication Mechanism*: During the exploration of the state-space Ω , the transition from a state $S = (\mathbf{e}_1, \dots, \mathbf{e}_{N_e})$ to a candidate solution $\tilde{S} = (\tilde{\mathbf{e}}_1, \dots, \tilde{\mathbf{e}}_{N_e})$ is controlled by a so-called communication mechanism [53], [54]. This mechanism, say Θ , is a Markov matrix on Ω whose entries $\Theta(S, \tilde{S})$ are the probabilities to move from a given state $S \in \Omega$ to a candidate solution $\tilde{S} \in \Omega$. Usually, the possible moves in Ω are defined via a neighborhood system \mathcal{G} on Ω , that is, $\mathcal{G} = \{\mathcal{G}(S) : S \in \Omega\}$, where the neighborhood $\mathcal{G}(S)$ of a state S is a subset of Ω such that: 1) $S \notin \mathcal{G}(S)$ and 2) $\tilde{S} \in \mathcal{G}(S) \iff S \in \mathcal{G}(\tilde{S})$ (in other words, a state cannot belong to its neighborhood and the neighborhood relation is symmetric). The mechanism Θ is then of the form

$$\Theta(S, \tilde{S}) = \begin{cases} \gamma \Gamma(S, \tilde{S}), & \text{if } \tilde{S} \in \mathcal{G}(S) \\ 1 - \gamma \sum_{S' \in \mathcal{G}(S)} \Gamma(S, S'), & \text{if } \tilde{S} = S \\ 0, & \text{otherwise} \end{cases} \quad (3)$$

where Γ is a positive function defined on $\{(S, \tilde{S}) \in \Omega \mid \tilde{S} \in \mathcal{G}(S)\}$ and γ is a positive constant that is small enough to guarantee that Θ is indeed a Markov matrix. In practice, Γ and γ are not defined explicitly; they are fixed implicitly by the implementation of the communication transitions. In our experiments, we use a simple neighborhood system defined as

$$\mathcal{G}(S) = \{\tilde{S} \in \Omega \mid \exists! k \in [1 \dots N_e], \tilde{\mathbf{e}}_k \neq \mathbf{e}_k\}. \quad (4)$$

In other words, $\mathcal{G}(S)$ is the set of arrays in Ω that differs from S in exactly one element, and Θ generates candidate solutions by changing one element at a time. This mechanism satisfies the symmetric support and irreducibility conditions required for the probabilistic convergence of SA (refer to [53] and [54] for the technical details).

The transition matrix $P(S_{n+1}|S_n)$ of the SA Markov chain $(S_n)_{n \in \mathbb{N}}$ is defined as

$$P(S_{n+1} = \tilde{S} | S_n = S) = \begin{cases} \Theta(S, \tilde{S}), & \text{if } \Delta U \leq 0 \text{ and } \tilde{S} \neq S \\ \Theta(S, \tilde{S}) \exp(-\beta_n \Delta U), & \text{if } \Delta U > 0 \end{cases} \quad (5)$$

where $\Delta U = U(\tilde{S}) - U(S)$ is the energy variation associated with the transition $S \rightarrow \tilde{S}$. In other words, a transition with negative energy variation is accepted unconditionally, whereas a transition with positive energy variation at iteration n is accepted with probability $\exp(-\beta_n \Delta U)$; this probability is called the acceptance rate. The annealing theory [53], [54] suggests to control this rate by a piecewise-constant cooling sequence $(\beta_n)_{n \in \mathbb{N}}$ of the form

$$\beta_n = \beta_{\text{inf}} \left(\frac{\beta_{\text{sup}}}{\beta_{\text{inf}}} \right)^{\frac{1}{\sigma-1} (\lceil \frac{n}{K} \rceil - 1)}, \quad (6)$$

where β_{inf} is the initial inverse temperature, β_{sup} is the final inverse temperature, $\lceil \cdot \rceil$ is the ceiling function, and σ is the number of constant temperature stages, each of length K (so the total number of iterations is $N_{\text{iter}} = \sigma K$).

3) *Energy Function*: The energy function U is the heart of the 2-D array design because its definition gives the objective to the optimization process. Here, the aim of the energy function U^{NH} is to control the shape of the BP at several depths in order to obtain an array that yields good image quality in terms of resolution (narrow beamwidth) and contrast (low SLL and GLL). To achieve this goal, the BP is simulated at several depths and at each depth a specific mask is designed to “sculpt” the shape of the BP.

a) *Beam pattern computation at several depths*: To compute the normalized beam pattern $\text{BP}_S(R, \theta, \phi)$ of the array S at iteration n , the associated emitted pressure field PF_S is first simulated using FIELDII [57], [58]

$$\text{BP}_S(R, \theta, \phi) = \frac{\max_t \text{PF}_S(R, \theta, \phi, t)}{\max_{\theta, \phi, t} \text{PF}_S(R, \theta, \phi, t)}, \quad (7)$$

where $\text{PF}_S(R, \theta, \phi, t)$ is the one-way emitted pressure field of S depending on spherical coordinates (R, θ, ϕ) and time t , the origin of which is the center of the probe layout.

As specified in [47], in order to simulate $\text{PF}_S(R, \theta, \phi, t)$, N_{PMP} pressure measurement points (PMPs) are positioned on a 3-D spiral arm lying on N_{H} hemispheres of radius $R_1, \dots, R_{N_{\text{H}}}$ so that no periodicity is introduced (or hidden) in the measurements. In the optimization, using several hemispheres of PMPs allows taking into account the pressure field behavior at focal depth d_{focus} , but also below and above d_{focus} . An example with $N_{\text{H}} = 3$ hemispheres is shown in Fig. 1.

Hence, multidepth energy functions can be defined and the acoustic radiation of the array can be optimized using simulations performed at different depths. When N_{H} hemispheres of PMPs are considered, the overall energy function is the weighted sum of the energy functions associated with each hemisphere

$$U^{\text{NH}}(S) = \sum_{i=1}^{N_{\text{H}}} \rho_i U_{R_i}(S), \quad (8)$$

with ρ_i the weight coefficient of the energy function value $U_{R_i}(S)$ computed at depth R_i .

b) *Sculpting the BP with a mask*: At each depth R where $\text{BP}_S(R, \theta, \phi)$ is simulated, a sculpting mask $\text{MASK}(R, \theta, \phi)$ is defined as follows to better control the ML shape and reduce the lateral lobes:

$$\text{MASK}(R, \theta, \phi) = \begin{cases} f(R, \theta), & \text{if } (\theta, \phi) \in L(R) \\ 0, & \text{if } (\theta, \phi) \notin L(R). \end{cases} \quad (9)$$

Here $L(R) = \{(\theta, \phi) | \theta < \theta_{\text{ML}}(R)\}$ is the ML region at depth R delimited by the angle $\theta_{\text{ML}}(R)$. Inside $L(R)$, MASK is given by the function $f(R, \theta)$, which will sculpt the ML shape while outside $L(R)$, MASK is set to zero in order to minimize the GLL and SLL. As a tool to define MASK, a graphical user interface was created to overlap the $\text{MASK}(R, \theta, \phi)$ over $\text{BP}_{\text{REF}}(R, \theta, \phi)$, the BP of any REF array chosen as reference. This tool can be used to adjust both the definition of the function $f(R, \theta)$ and the angle $\theta_{\text{ML}}(R)$ at each depth R .

To make the ML shape fit under $\text{MASK}(R, \theta, \phi)$ and concentrate the acoustic energy inside $L(R)$, $U_R(S)$ is defined as the square of the product between $M(R)$, the maximum of pressure above $\text{MASK}(R, \theta, \phi)$, and the pressure ratio $P_{\text{out}}(R)/P_{\text{in}}(R)$, respectively

$$U_R(S) = \left(M(R) \left(\frac{P_{\text{out}}(R)}{P_{\text{in}}(R)} \right) \right)^2, \quad (10)$$

with

$$P_{\text{out}}(R) = \iint_{(\theta, \phi) \notin L} (\text{BP}_S(R, \theta, \phi))^2 d\theta d\phi, \quad (11)$$

and

$$P_{\text{in}}(R) = \iint_{(\theta, \phi) \in L} (\text{BP}_S(R, \theta, \phi))^2 d\theta d\phi. \quad (12)$$

B. Simulated Annealing Workflow

Once the state-space Ω , the communication mechanism Θ , and the energy function U are defined, the number of iterations N_{iter} can be chosen based on the time and computational power available. The flowchart given in Fig. 2 summarizes the different steps of the SA algorithm.

- 1) Random choice of the initial solution $S_0 \in \Omega$ and computation of the initial pressure field $\text{PF}_{S_0}(R, \theta, \phi, t)$ and associated energy $U^{\text{NH}}(S_0)$. The initial and final inverse temperatures β_{inf} and β_{sup} are computed using the methods described in [53] and [54].
- 2) Generation of a new solution \tilde{S}_n using the communication mechanism Θ described in Section II-A2.
- 3) Acoustic simulation using FIELD II to compute the PF update associated with the candidate solution \tilde{S}_n .
- 4) Computation of the energy difference ΔU between the current solution S_n and the candidate solution \tilde{S}_n .
- 5) Acceptation or rejection of the candidate solution: \tilde{S}_n is accepted with probability $\min(\exp(-\beta_n \Delta U), 1)$.
- 6) Update of the iterate S_{n+1} , which is either \tilde{S}_n or S_n depending on the decision taken in step 5.
- 7) Update of the iteration index and the inverse-temperature value.

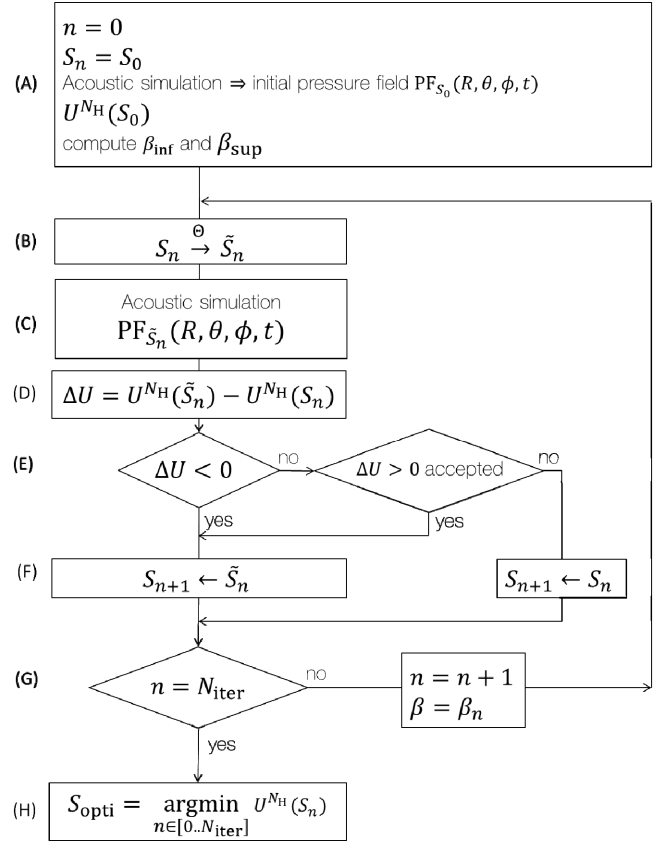


Fig. 2. SA flowchart.

- 8) Output of the best solution S_{opti} encountered during the optimization process.

In sum, the energy function U specifies the goals in terms of the acoustic performance (see Section II-A3) and the search for the optimal array is performed by exploring the finite state-space Ω (see Section II-A1) using the communication mechanism Θ (see Section II-A2). The specificity of SA is that the probability to accept a transition $S \rightarrow \tilde{S}$ [step (E) in Fig. 2] is controlled by a cooling sequence $(\beta_n)_{n \in \mathbb{N}}$.

III. CASE STUDY: FINDING THE BEST CONFIGURATION OF N_e ACTIVE ELEMENTS IN AN $N_x N_y$ 2-D ARRAY

A. State Space and Design Constraints

1) *1024-Element Reference Array*: Let us consider a generic 2-D matrix with $N_x N_y$ elements (N_x columns by N_y rows of elements) and a scanner with $N_e \ll N_x N_y$ independent channels. Assuming that neither multiplexing nor microbeamforming is used, N_e can be set equal to the number of independent channels that are usually available in clinical and research US scanners, i.e., $N_e = \{128, 192, 256\}$. In this example study, any full 2-D matrix with $N_x N_y$ elements can be considered. In particular, we focus on ref1024 (one of the two references considered for the experimental validation), the effective planar matrix architecture of a 1024 ($N_x = N_y = 32$) active elements probe (Fig. 3) manufactured by Vermon (Tour, France). The central frequency is 3 MHz (bandwidth 72%), the elements are squares 249 μm wide, and the pitch (distance

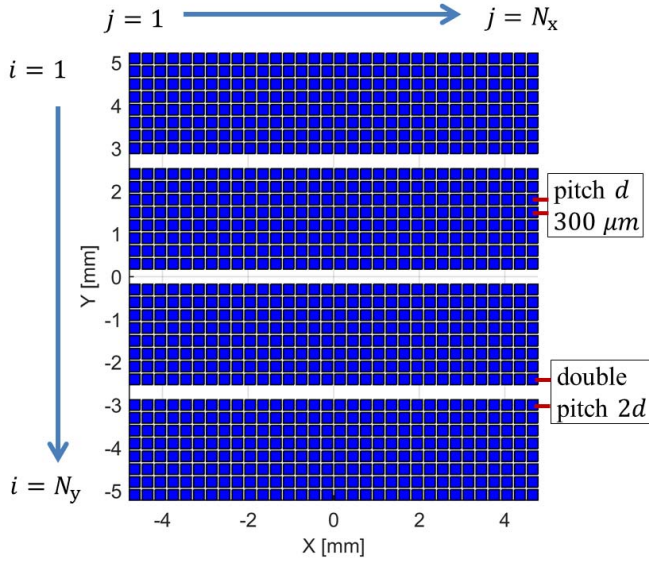


Fig. 3. Layout of the 32×32 element 2-D array matrix ref1024 with double pitch distance between lines 8–9, 16–17, and 24–25 to facilitate the electronic connections as described in [15].

between consecutive elements centers) is $d = 300 \mu\text{m}$ in both the x - and y -directions. Assuming that ref1024 is a gridded 2-D array, the k th element is indexed as the one located on the i th line ($i \in [1..N_y]$) and j th column ($j \in [1..N_x]$) of ref1024 using $k = i + (j - 1)N_y$, so that $k \in [1..N_x N_y] = [1..1024]$. The elements of ref1024 are $(\mathbf{e}_1, \dots, \mathbf{e}_{N_x N_y})$ are of the form (2), where the components other than the positions (x_k, y_k, z_k) and the transmission delays τ_k are fixed in accordance with the probe specifications: the element size is set to $a_k = 249 \mu\text{m}$, the element orientation is set to $(\theta_k, \phi_k) = (0, 0)$, the element weight is set to $w_k = 1$ (no apodization is applied to maximize the sensitivity of the array), the impulse response Imp_k is implemented by sampling at $F_s = 30 \text{ MHz}$ a 2.5-sine cycles at 3 MHz weighted by Hanning window, and the excitation signal Exc_k is implemented by sampling at $F_s = 30 \text{ MHz}$ a 3-sine cycles at 3 MHz weighted by Hanning window (62% bandwidth).

As mentioned in [15], the effective matrix architecture of ref1024 integrates a double pitch distance between the lines $n^\circ 8$ - $n^\circ 9$, $n^\circ 16$ - $n^\circ 17$, and $n^\circ 24$ - $n^\circ 25$ to facilitate the electronic connection (wiring pathway) of the piezoelectric elements. It results that, along the y -direction, $N_d = 3$ deactivated lines (not indexed) are empty of elements (Fig. 3). The k th element (located on the i th line and j th column) has the following position coordinates:

$$\begin{cases} x_k = \left(j - \frac{N_x + 1}{2} \right) d, \\ y_k = \left(\frac{N_x + N_d + 1}{2} - \left(1 + \left\lfloor \frac{i-1}{8} \right\rfloor \right) \right) d, \\ z_k = 0, \end{cases} \quad (13)$$

where $\lfloor \cdot \rfloor$ is the floor function.

The transmission delay τ_k is computed as follows, considering a focal point at 40 mm on the z -axis:

$$\tau_k = \frac{1}{c} \left(\sqrt{x_f^2 + y_f^2 + z_f^2} - \sqrt{(x_k - x_f)^2 + (y_k - y_f)^2 + (z_k - z_f)^2} \right), \quad (14)$$

where $c = 1540 \text{ m/s}$ is the speed of sound and $(x_f, y_f, z_f) = (0, 0, 40) \text{ mm}$ is the position of the focal point.

2) *716-Element Reference Array*: It is known that homogeneous radiating performance (with respect to the ϕ angle) is favored using circular footprints [28], [29], [32], [34]. Hence a circular reference array ref716 was introduced for validation. This 716-element circular array results from the deactivation of the elements in ref1024 that are outside a disk of radius 4.8 mm (centered $x = 0, y = 0$). The diameter of the ref716 aperture was chosen equal to the shorter side of ref1024 to produce a circular footprint. The consequence of corner elements deactivation is that the secondary lobe energy along the axis of the array is reduced at the expense of a wider ML.

3) *Effective State Space*: The state-space Ω is based on ref1024 (the corner elements are available during the optimization): Ω is isomorphic to the set of N_e -permutations of $\{\mathbf{e}_1, \dots, \mathbf{e}_{N_x N_y}\}$. Indeed, $S = (\mathbf{e}_{k_1}, \dots, \mathbf{e}_{k_{N_e}}) \in \Omega$ if and only if $k_u \in [1..1024]$ for all $u \in [1..N_e]$ and $k_u \neq k_v$ if $u \neq v$. In a nutshell, a given solution $S \in \Omega$ is a 2-D sparse array with N_e active elements in the full 1024-elements matrix array.

B. Communication Mechanism

In this example study, the communication mechanism Θ is implemented by moving a single element from its current position to an available (i.e., nonactive) neighboring position in an eight nearest spatial neighborhood system. This spatial neighborhood system enters into the definition but should not be confused with the communication neighborhood system \mathcal{G} defined in Section II-A2: for every array S , $\mathcal{G}(S)$ is the set of arrays \tilde{S} that differ from S in exactly one element $\tilde{\mathbf{e}}_k$ located in an available position in the eight nearest spatial neighborhood of \mathbf{e}_k .

Because of the boundary constraints, the number of candidate positions around a given element depends on the spatial location of this element: three in a corner, five on the border, and eight elsewhere. The double pitch separating the elements of lines $n^\circ 8$ - $n^\circ 9$, $n^\circ 16$ - $n^\circ 17$, and $n^\circ 24$ - $n^\circ 25$ has no impact on the neighborhood structure, as if there were no gaps. Any no-occupied position in an element neighborhood can be picked up with the same probability, and the occupied neighboring positions cannot be selected.

C. Energy Function

A specific array design for echocardiography is presented to illustrate the general method (notations are defined in Section II-A3). In this example study, we set $N_H = 3$ and $N_{\text{PMP}} = 3000$ with $R_1 = 30 \text{ mm}$, $R_2 = 40 \text{ mm}$ (focal depth) and $R_3 = 50 \text{ mm}$ (Fig. 1). To define U_R , the sculpting function $f(\theta, R)$ and the angle $\theta_{\text{ML}}(R)$ (delimiting the ML region) are computed at each depth using the graphical user interface (see Fig. 4) with ref1024 as the reference [designated as

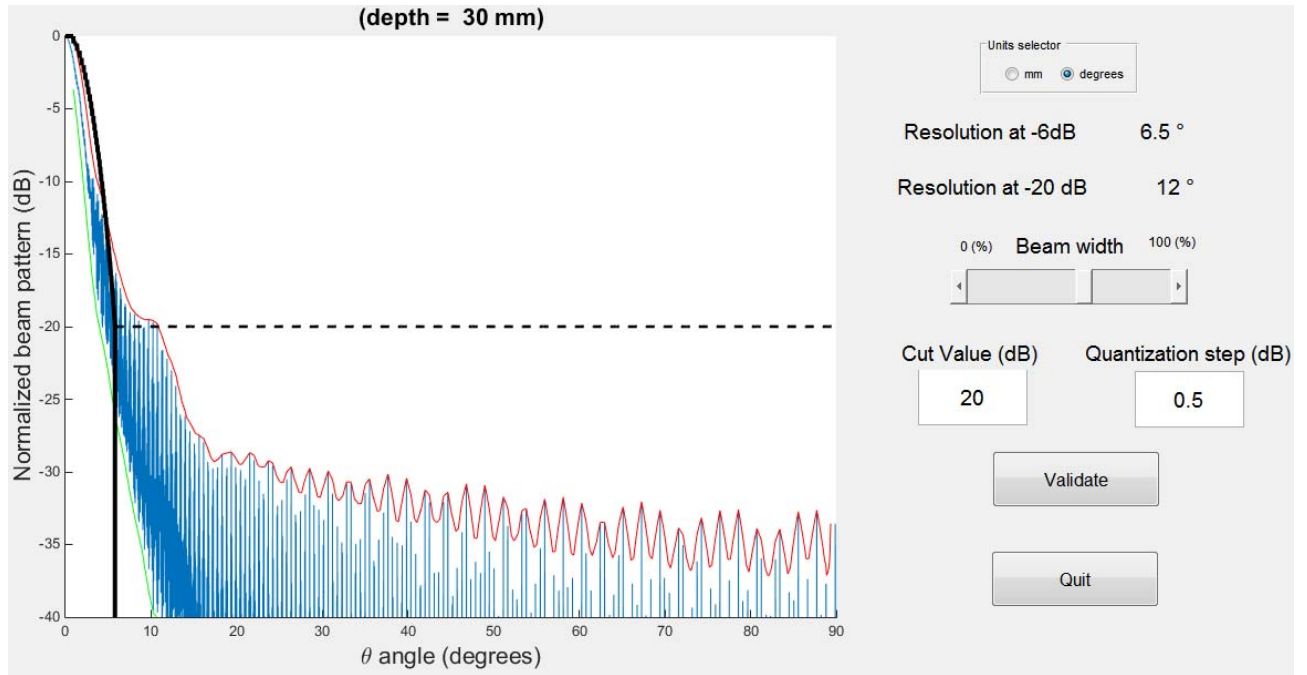


Fig. 4. Screenshot of the graphical user interface used to define the sculpting mask shape based on the BP of the 1024-element reference array ref1024: the blue line gives the BP value for each PMP and the red line is the worst case envelope. The beamwidth constraint, the cut value $C(R)$ (dotted black line), and the quantization step q_{mask} can be interactively adjusted to define the shape of the sculpting mask (full black line) at each depth where the BP is simulated.


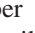
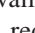
REF in Section II-A3b)] (ref1024 was used instead of ref716 because it represents the set of available positions for the N_e elements during the optimization). The function $f(\theta, R)$ is defined as the inverse Fourier transform of a Nuttall window [59]. Then $\theta_{\text{ML}}(R)$ is computed as the beamwidth of $f(\theta, R)$ at $-C(R)$ dB where $C(R)$ is the cut value at depth R . The GUI allows adjusting interactively both the Nuttall window size and the cut value $C(R)$ so that it is related with reference BP_{ref1024}(R, θ, ϕ) over which the MASK is displayed (Fig. 4). Finally, the resulting MASK is quantized by steps of q_{mask} dB to avoid a too strict ML constraint for very small values of θ .

In this example study, the cut value was the same at the three depths: $C(R_1) = C(R_2) = C(R_3) = -20$ dB and the size of the Nuttall window was adjusted, at each depth, to be close to the resolution yielded by ref1024 at focal depth R_2 . Hence, the ML regions $L(R_1)$, $L(R_2)$, and $L(R_3)$ were delimited by $\theta_{\text{ML}}(R_1) = 6.0^\circ$, $\theta_{\text{ML}}(R_2) = 5.4^\circ$, and $\theta_{\text{ML}}(R_3) = 6.9^\circ$ which are, respectively, 56% (R_1), 105% (R_2), and 125% (R_3) of the half beamwidths at -20 dB of ref1024. Incidentally, it corresponds to 98% (R_1), 150% (R_2), and 148% (R_3) of the respective half beamwidths at -20 dB of ref716. The quantization step was set to be $q_{\text{mask}} = 0.5$ dB.

To sum up, each value of U_R was computed as specified in (8) and the overall energy function U^{NH} was the equi-weighted sum of the energy function values associated with each hemisphere

$$U^{\text{NH}} = \sum_{i=1}^{N_{\text{H}}} U_{R_i}. \quad (15)$$

D. Optimization Setup

The optimization process was launched thrice with the setup described above and a number of elements $N_e = \{128, 192, 256\}$ to obtain three optimized sparse arrays hereafter designated as opti128 , opti192 , and opti256 , respectively. The number of iterations $N_{\text{iter}} = \sigma K$ was fixed by dividing the available computation time (168 h – one week) by the time required to complete a single iteration (0.46 s). In order to give to all of the elements a chance to be moved during each of the σ temperature stages, K was set equal to N_e and σ resulted equal to 5000. Thanks to a speedup of the PF update [47], the number of iterations N_{iter} achievable in a given amount of time is about 70 times greater than that with a standard implementation.

E. Performance Analysis

1) *3-D Beam Pattern*: Three-dimensional one-way pressure fields were simulated in a 3-D volume ($L_x \times L_y \times L_z = 100 \times 100 \times 40 \text{ mm}^3$) for each optimized array. The simulated volume was centered over the array starting at depth $z = 20$ mm and it was sampled with a voxel resolution of $v_{\text{res}} = \delta x \times \delta y \times \delta z = 667 \times 667 \times 667 \text{ } \mu\text{m}^3 = 0.43\lambda^3$. For each solution, 81 steering angles ($\theta_{z_x} = -32 : 8 : +32^\circ$, $\theta_{z_y} = -32 : 8 : +32^\circ$) were considered, and for each simulation the array performance was assessed through the following parameters [25].

- 1) *SLL*: Log compressed ratio between the intensities of the highest secondary lobe and the ML.

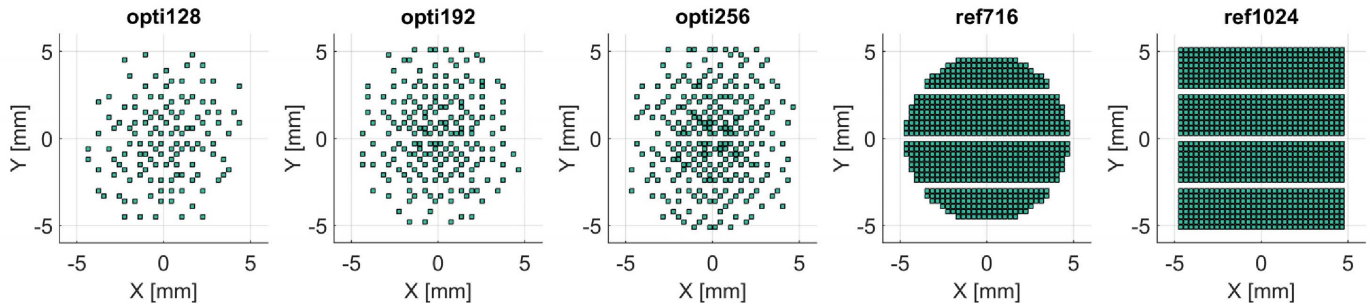


Fig. 5. Layouts of the optimization results opti128, opti192, opti256, and the two reference arrays ref716 and ref1024. The corner elements deactivation happened spontaneously during the optimization of opti128, opti192, and opti256, whereas it was artificially imposed for ref716.

- 2) *Lateral Resolution*: Average -6 dB width of the main beam (FWHM) in a plane perpendicular to the US propagation direction.
- 3) *Depth of Field (DOF)*: -6 dB length along the steering direction.
- 4) *Sidelobe to ML Energy Ratio (SMER)*: Log compressed ratio between the average intensity outside and inside the focal region, i.e., the region surrounding the focus delimited by the -6 dB isosurface.
- 5) *Sensitivity*: Focus intensity normalized on the reference array ref1024.

The corresponding simulation results are presented in Section IV-C where the boxplots illustrate the distribution of the performance over the 81 tested steering angles.

2) *3-D Imaging*: The imaging capability of optimized and reference arrays are compared using a resolution phantom and a contrast phantom. For each array and each phantom, two orthogonal B-mode images (xz plane when $\phi = 0$ and yz plane when $\phi = 90^\circ$) were reconstructed with a 90° sector angle coverage ($-45^\circ, +45^\circ$) and a maximum depth of 70 mm. The 90° sector was scanned transmitting 180 beams, focused at depth 40 mm, with a 0.5° step between each steering angle. For each transmitted beam, a dynamic focalization was applied in reception to beamform the corresponding line in the image. The sector scan images were finally computed as the log compression of the interpolated 180 postbeamforming RF-lines.

The resolution phantom consists of five scatterers equispaced by 5 mm along the z -axis, with the middle one at the 40 mm focal depth. The lateral resolution was evaluated as the FWHM of the point spread functions of these scatterers. To qualitatively assess the imaging capability of the arrays with a 30° steering angle, four additional scatterers were added in the phantom at the respective positions $\{(-23, 0, 40), (23, 0, 40), (0, -23, 40), (0, 23, 40)\}$ mm.

The contrast phantom consists of a 3-D anechoic cyst of radius 7.5 mm located at 40 mm depth. A total of 1 750 000 scatterers were randomly placed in a volume delimited by $x = [-25, 25]$ mm, $y = [-25, 25]$ mm, and $z = [20, 60]$ mm (see Section IV-D). Considering the resolution cell of ref1024 at the focal point, it corresponds to 19.6 scatterers per resolution cell of 1.12 mm^3 .

The contrast-to-noise ratio (CNR) was computed according to

$$\text{CNR} = 20 \log_{10} \left(\frac{|\mu_{\text{in}} - \mu_{\text{out}}|}{\sqrt{(\sigma_{\text{in}}^2 + \sigma_{\text{out}}^2)/4}} \right) \quad (16)$$

where $\mu_{\text{in}}/\mu_{\text{out}}$ and $\sigma_{\text{in}}/\sigma_{\text{out}}$ correspond to the respective mean and standard deviation of the B-mode image module inside/outside the cyst. For the evaluation, the inside region was delimited by a circle of radius 7.45 mm. The outside region of the cyst was delimited by an inner circle of radius 7.55 mm and an outer circle of radius 9 mm.

3) *Robustness*: To test if the presented results were robust when changing the initial state S_0 , the same optimization setup was performed ten times, each time starting from a different initial state. Owing to the identical optimization setup the ten obtained results are designated as “clones.” The optimization setup was identical to that used with opti256 but the ML regions $L(R_1)$, $L(R_2)$, and $L(R_3)$ were, respectively, delimited by $\theta_{\text{ML}}(R_1) = 4.1^\circ$, $\theta_{\text{ML}}(R_2) = 5.0^\circ$, and $\theta_{\text{ML}}(R_3) = 6.5^\circ$, which are 75%, 106%, and 135% of the half beamwidths at -20 dB of opti256 at the same depths R_1 , R_2 , and R_3 . The motivation and the impact of the resolution constraint strengthening at depth R_1 (while relaxing at depth R_3) is discussed in Section V-E.

IV. RESULTS

A. Layouts and Energy Function Values

The layouts obtained with solutions opti128, opti192, opti256, and the reference arrays ref716 and ref1024 are presented in Fig. 5.

Qualitatively, the optimized layouts do not respect any periodic pattern but they seem to present a circular symmetry. The distances of the layouts barycenter with respect to the origin are 0.2λ , 0.47λ , and 0.08λ for the respective arrays opti128, opti192, opti256, and 0λ for both ref716 and ref1024. It can be noticed that the apertures opti128, opti192, and opti256 are confined in disks of radius 5.3, 5.6, and 5.7 mm, respectively: the confinement of the elements in a disk shape was not forced (the corner elements were available during the optimization), but they were spontaneously deactivated by the optimization process itself. On the contrary, the circular array

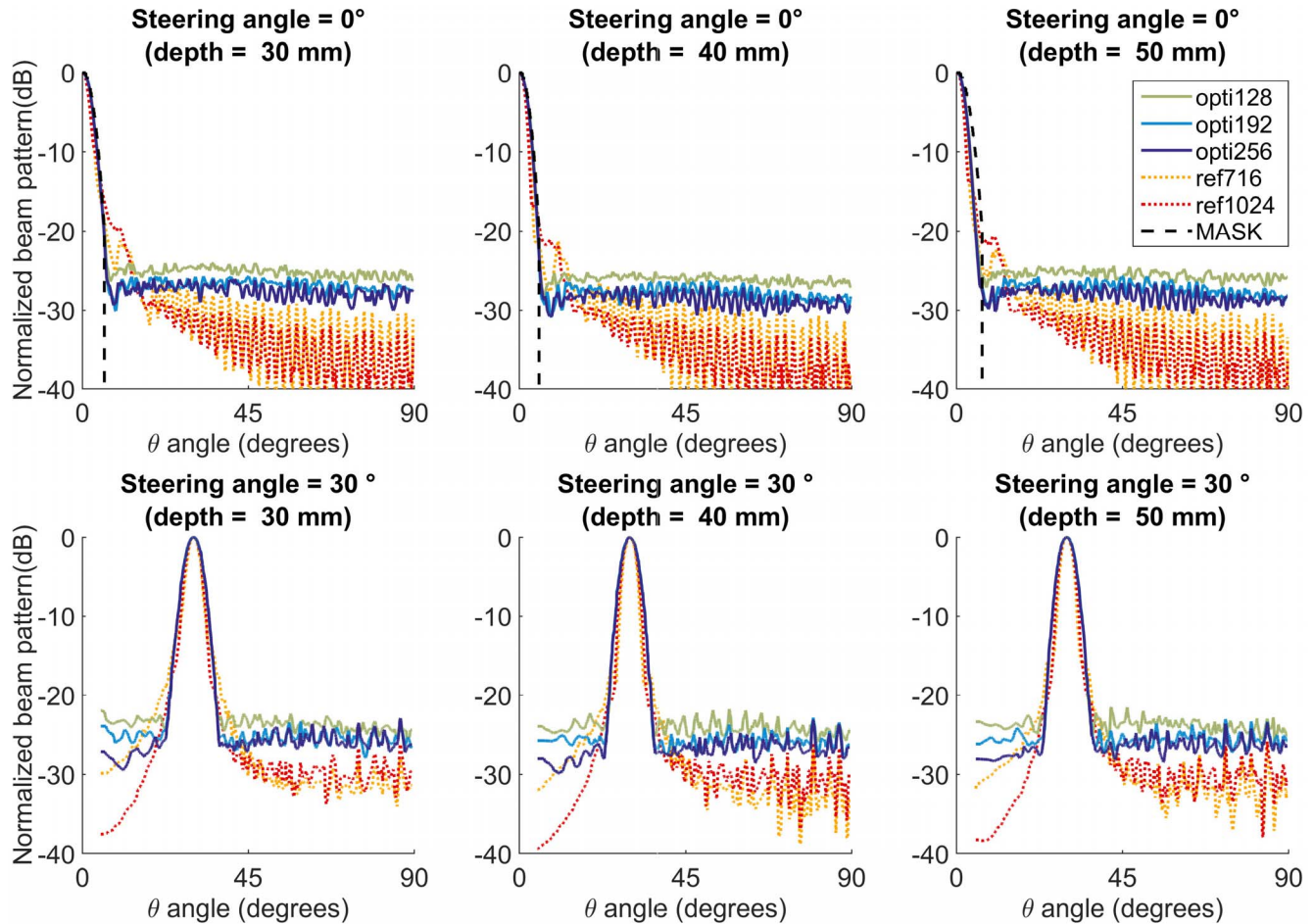


Fig. 6. Radiated BPs (worst case) at depths 30 (left), 40 (center), and 50 mm (right) of the optimization results and the reference arrays ref716 and ref1024. The constraints MASK is shown in black dashed lines. The steering angles were 0° (top panels) and 30° (bottom panels).

TABLE I
ENERGY FUNCTION VALUES ASSOCIATED WITH THE OBTAINED SOLUTIONS Opti128, Opti192, Opti256, AND THE REFERENCE ARRAYS Ref716 AND Ref1024

	opti128	opti192	opti256	ref716	ref1024
$U^{NH} (\times 10^6)$	39.9160	8.3111	3.7274	3.7265	7.3400

ref716 was produced from ref1024 by intentionally removing the corner elements outside a disk of radius 4.8 mm (maximum size of ref1024 along the x -axis, see Section III-A2).

The energy function values U^{NH} (opti128), U^{NH} (opti192), U^{NH} (opti256), U^{NH} (ref716), and U^{NH} (ref1024) are reported in Table I. The energy value decreases with the number of elements for the optimized results. The energy value U^{NH} (opti256) is very close but slightly higher than that obtained with ref716. On the contrary, U^{NH} (ref1024) is higher than U^{NH} (opti256). The fact that ref1024 is not associated with the best score is discussed in Section V-B.

B. Comparison of the Multidepth Beam Patterns

The BP of opti128, opti192, opti256, ref716, and ref1024 are qualitatively compared in Fig. 6 for both the

steered (bottom) and not steered (top) cases at the three depths of interest ($R_1 = 30$ mm, $R_2 = 40$ mm, and $R_3 = 50$ mm). The BPs of the optimized arrays fit, at all depths, below the sculpting MASK, which is plotted (black dashed lines) in Fig. 6 [see Section II-A3b) for the definition of MASK]. The BP MLs of the optimized arrays are followed by a flat *plateau* up to $\theta = 90^\circ$. For all the optimized arrays and at all depths, when a steering angle of 30° is applied, the ML shape is very regular and the flat *plateau* can still be observed (no grating lobes). The BP of both reference arrays (ref716 and ref1024) present sidelobes close to the ML (around 10°) that tend to rapidly decrease. A more detailed illustration of the optimized arrays BP and reference arrays BP at depths R_1 , R_2 , and R_3 is displayed, with a 40-dB dynamic range in Fig. 7 when no steering is applied, and in Fig. 8 when a 30° steering angle is applied. In both Figs. 7 and 8, it can be noticed that for ref1024 sidelobes over -40 dB are present along the x - and y -directions, whereas for ref716 they are only present along the y -direction. For the optimized arrays such sidelobes are homogeneously spread over the entire hemisphere (there is no worst case direction).

A quantitative comparison of the BPs can be done thanks to Table II which gives the SLL (peak and average values measured outside L) and the -6 and -20 dB ML widths for

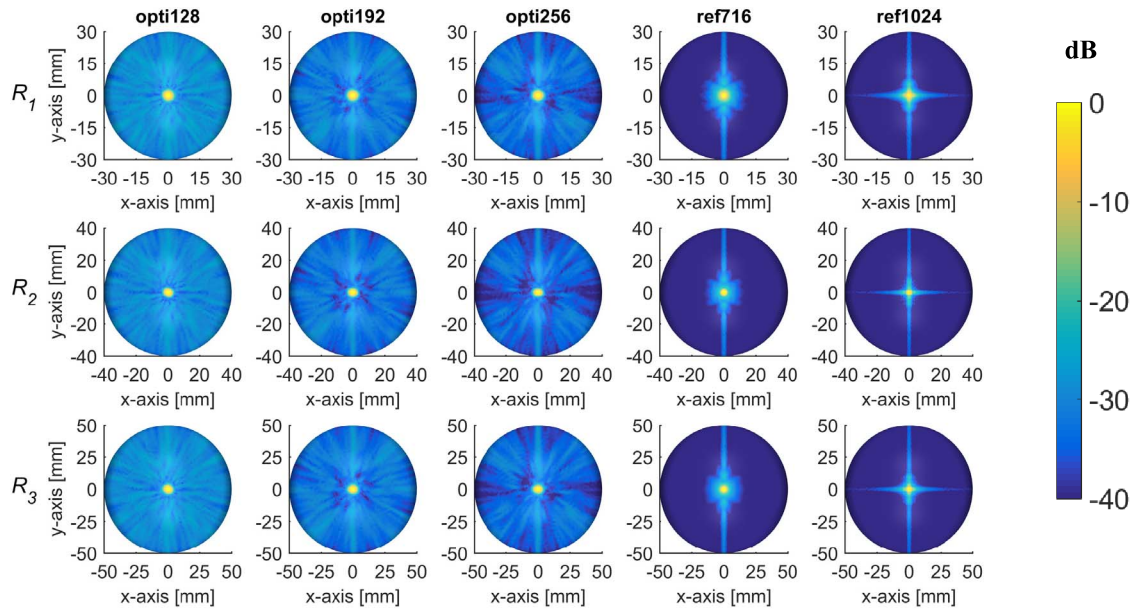


Fig. 7. Radiated BPs (no steering) of the optimized arrays and the reference array evaluated on the three hemispheres at depths 30 (bottom line), 40 (middle line), and 50 mm (top line).

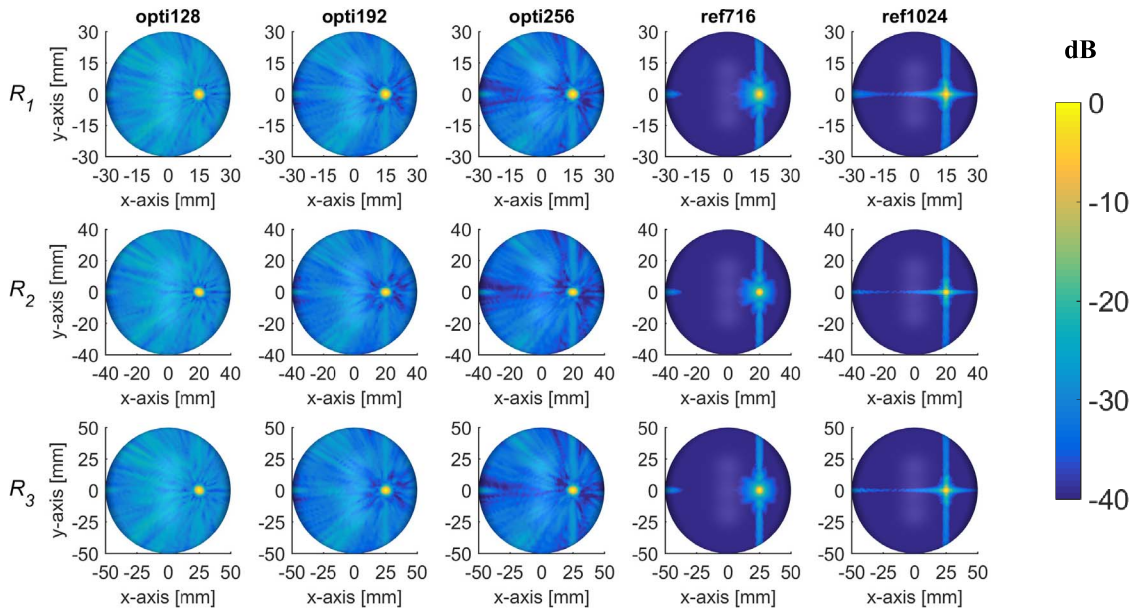


Fig. 8. Radiated BPs (steering of 30°) of the optimized arrays and the reference array evaluated on the three hemispheres at depths 30 (bottom line), 40 (middle line), and 50 mm (top line).

each of the optimized and reference arrays. The “peak SLL” (designated as usual by SLL) is defined as a ratio between the ML maximum value and the highest sidelobe value. By contrast the “average SLL” (SLL_{ave}) is defined as the log-compressed average of the BP (linear values) outside L .

The best SLL performance is obtained by opti256 at the three depths. Compared to opti128, the SLL of opti256 is 1.9, 1.8 and 2.2 dB lower at depths R_1 , R_2 , and R_3 , respectively. Compared to opti192, the SLL of opti256 is 0.3 dB (R_1), 0.7 dB (R_2), and 0.9 dB (R_3) lower. The SLL obtained by ref1024 is 6.5 dB (R_1), 10.3 dB (R_2), and 12.9 dB (R_3)

higher than with opti256. The SLL obtained by ref716 is still 4.8 dB (R_1), 5.7 dB (R_2), and 4.2 dB (R_3) higher than with opti256.

The same trend with the SLL_{ave} is observed among the optimized arrays, where opti256 overmatches the performance of opti128 of 4.5 dB (R_1), 4.8 dB (R_2), and 4.9 dB (R_3). Compared to opti192, the SLL_{ave} of opti256 is 1.7 dB (R_1), 1.8 dB (R_2), and 1.9 dB (R_3) lower. Contrary to the SLL, ref1024 shows the best SLL_{ave} performance, which is 9.9 dB (R_1), 11.9 dB (R_2), and 12.4 dB (R_3) lower than with opti256. Similar to ref1024, ref716 yields SLL_{ave} performance

TABLE II
SLL AND ML WIDTH EVALUATED ON HEMISPHERES OF RADIUS 30, 40, AND 50 mm OBTAINED FOR THE OPTIMIZED AND REFERENCE ARRAYS. THE BEST PERFORMANCE IN EACH COLUMN IS HIGHLIGHTED IN GREEN

	Side Lobe Level (in dB)						Main Lobe Width at -6dB and -20dB (in degree)					
	$R_1 = 30$ mm		$R_2 = 40$ mm		$R_3 = 50$ mm		$R_1 = 30$ mm		$R_2 = 40$ mm		$R_3 = 50$ mm	
	SLL	SLL _{ave}	SLL	SLL _{ave}	SLL	SLL _{ave}	at -6 dB	at -20 dB	at -6 dB	at -20 dB	at -6 dB	at -20 dB
opti128	-24.1	-28.4	-25.1	-29.4	-24.4	-28.8	5.4	11.6	5.2	9.4	5.2	10.0
opti192	-25.7	-31.2	-26.2	-32.4	-25.7	-31.8	5.5	10.9	5.1	9.2	5.2	9.6
opti256	-26.0	-32.9	-26.9	-34.2	-26.6	-33.7	5.4	11.1	5.2	9.4	5.0	9.6
ref716	-21.2	-39.7	-21.2	-41.6	-22.4	-42.0	4.7	12.2	4.3	7.2	4.3	9.3
ref1024	-19.5	-42.8	-16.6	-46.1	-13.7	-46.1	4.0	21.4	3.6	10.2	3.7	11.1

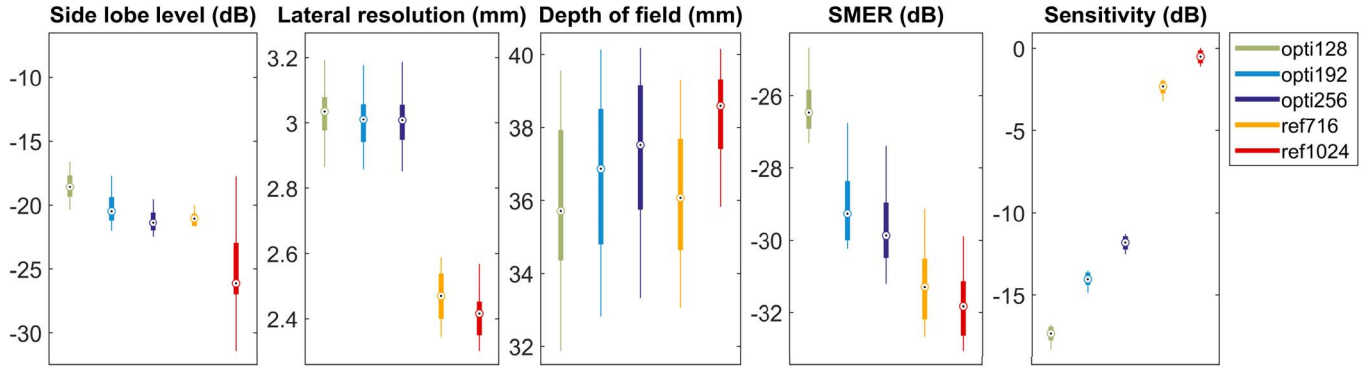


Fig. 9. SLL, lateral resolution, DOF, SMER, and sensitivity from the 3-D BP analysis (statistics over 81 steering angles). The plotted whisker extends to the adjacent value, which is the most extreme data value that is not an outlier. Outliers are beyond the 99.3 coverage (normal distribution).

which is 6.8 dB (R_1), 7.4 dB (R_2), and 8.3 dB (R_3) lower than with opti256. For all optimized arrays, both SLL and SLL_{ave} are always lower at depth R_2 (focal depth) than at depths R_1 and R_3 .

The resolution at -6 dB is very close for all the optimized arrays with mean 5.4° (R_1), 5.2° (R_2), and 5.1° (R_3). The best resolution at -6 dB is yielded by ref1024 which overmatches by 1.4° (R_1), 1.6° (R_2), and 1.3° (R_3) the -6 dB resolution of opti256. The -6 dB resolution obtained with ref716 is also slightly better than with opti256 of 0.7° (R_1), 0.9° (R_2), and 0.7° (R_3).

The resolution at -20 dB is very similar for all the optimized arrays with mean 11.2° (R_1), 9.3° (R_2), and 9.7° (R_3). Contrary to the resolution at -6 dB, ref1024 has the coarsest resolution at -20 dB with $+10.3^\circ$ (R_1), $+0.8^\circ$ (R_2), and $+1.5^\circ$ (R_3) compared to opti256. The situation is quite different for ref716, which yields the best -20 dB resolution performance at both R_2 (7.2°) and R_3 (9.3°) but at depth R_1 it is slightly coarser ($+1.3^\circ$) than opti192 (the latter has yields the best -20 dB resolution at this depth).

C. 3-D Beam Patterns Analysis Over 81 Steering Angles

Qualitatively, the performance evaluated on the 3-D BP (Fig. 9) improves with the number of elements. A quantitative analysis of the 3-D acoustic performance over 81 steering angles can be done from Fig. 9. In terms of SLL, the best median value is obtained by ref1024 (-26.1 dB) but high peaks can be noticed for extreme steering angles. Moreover for ref1024, an SLL of -17.7 dB is observed when no steering is applied which is consistent with the SLL values

reported in Table II. On the contrary, ref716 yields a SLL performance with -21 dB median value with a very small range of variation with the steering angles (see discussion in Section V-C). Compared to ref716, the median SLL of opti128 and opti192 is, respectively, 2.5 and 0.6 dB higher while opti256 yields a slightly better SLL median value (-21.4 dB). The references ref716 and ref1024 have a median lateral resolution of 2.5 and 2.4 mm, respectively. Compared to ref1024, the median lateral resolution of all the optimized arrays is 0.6 mm coarser. In terms of DOF, the best performance is also achieved by ref1024 (38.6 mm) which overcomes ref716 (36.1 mm) of 2.5 mm. Compared to ref1024, the median DOF of opti128, opti192, and opti256 is, respectively, 2.9, 1.7, and 1.1 mm shorter. The best median value of SMER is obtained by ref1024 which is 0.5 and 1.96 dB lower than with ref716 and opti256, respectively. The SMER yielded by opti256 is itself 3.5 and 0.6 dB lower than opti128 and opti192, respectively. Compared to ref1024, the median sensitivity of opti128, opti192, opti256, and ref716 is, respectively, 17.1, 13.5, 11.3, and 1.8 dB lower.

D. Image Simulations

Qualitatively, the resolution (Fig. 10) appears to be very similar for all of the optimized arrays and ref716. The images in Fig. 11 clearly show that the contrast improves with the number of elements. Quantitatively, it can be seen from Table III that the best lateral resolution is obtained by ref1024 in both the xz (1.7 mm) and yz (1.4 mm) planes. For the optimized arrays, the resolution in both the xz and yz planes is in average 40% coarser than for ref1024. The resolution of

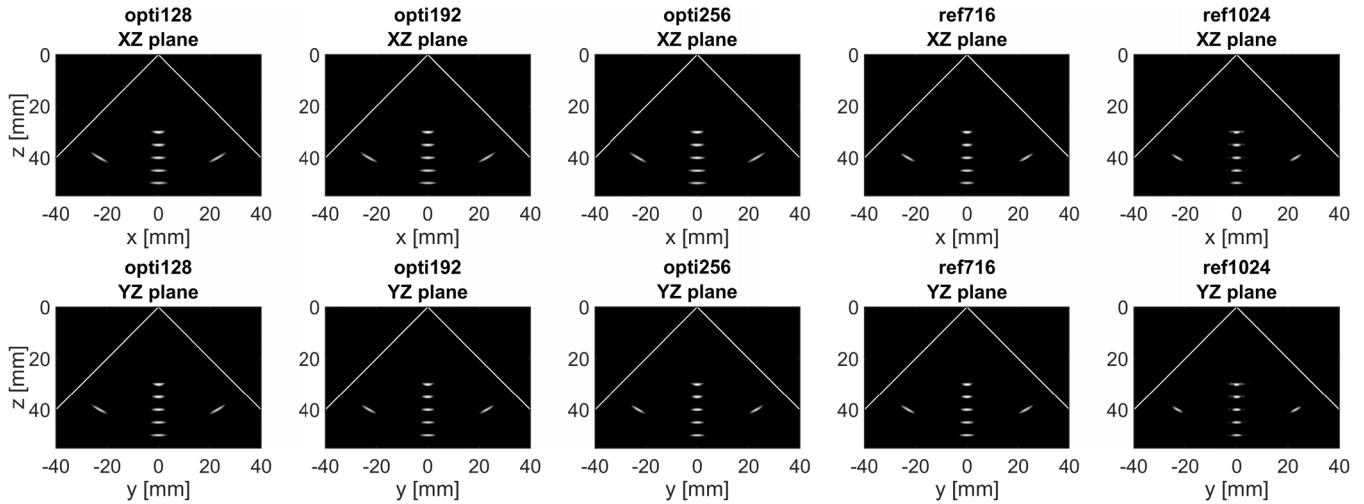


Fig. 10. Resolution images (xz plane at the top and yz plane at the bottom) of a resolution phantom containing five equidistant scatterers along z -axis from 30 to 50 mm in depth. The dynamic range is 40 dB.

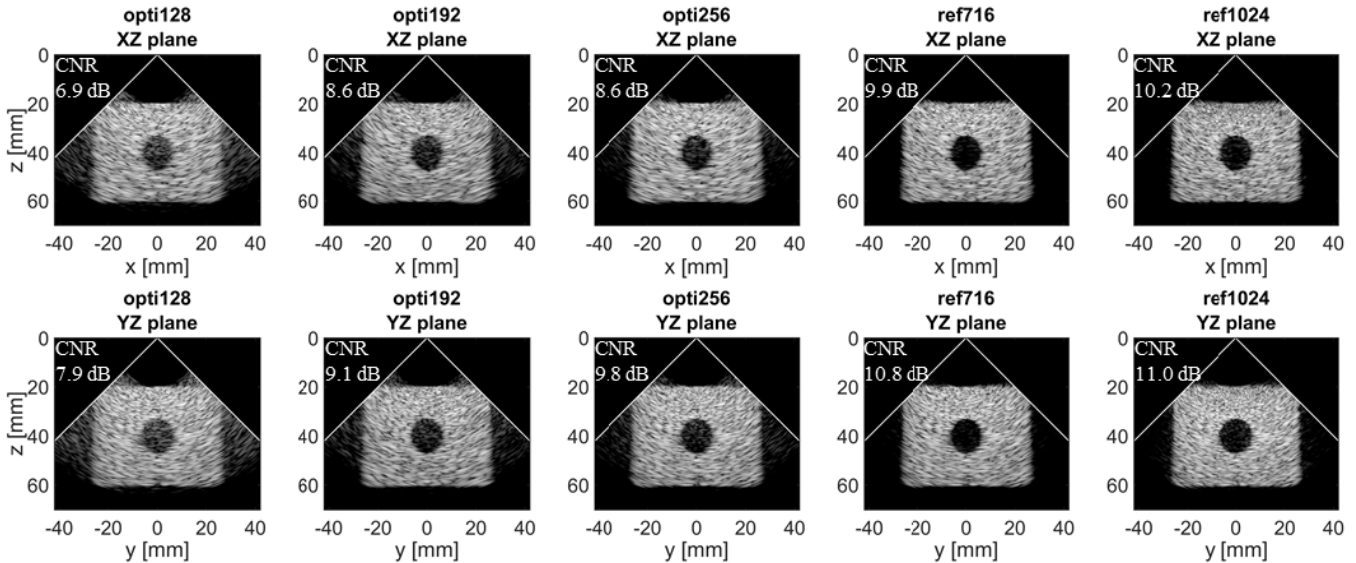


Fig. 11. Contrast images (xz plane at the top and yz plane at the bottom) of an anechoic cyst phantom of radius 7.5 mm located at 40 mm depth. The dynamic range is 40 dB.

TABLE III
LATERAL RESOLUTION AT -6 dB AND CNR EVALUATED ON IMAGE SIMULATIONS FOR THE OPTIMAL ARRAYS AND THE REFERENCE. THE BEST PERFORMANCE IN EACH COLUMN IS HIGHLIGHTED IN GREEN

	Lateral resolution at -6 dB (mm)		CNR (dB)	
	(average on the 5 scatterers)		Cyst ($z = 40$ mm, $r = 7.5$ mm)	
	XZ	YZ	XZ	YZ
opti128	2.3	2.3	6.9	7.9
opti192	2.4	2.1	8.6	9.1
opti256	2.5	1.9	8.6	9.8
ref716	2.3	2.3	9.9	10.8
ref1024	1.7	1.4	10.2	11.0

ref716 equals that of opti128 in both the xz (2.3 mm) and yz (2.3 mm) planes. The relatively coarse resolution of ref716 compared to ref1024 is discussed in Section V-D. On the contrary, in terms of contrast the CNR of ref716 is very close

to that of ref1024 in both the xz (-0.3 dB) and yz planes (-0.2 dB). The CNR of opti128, opti192, and opti256 is 3.0, 1.3, and 1.3 dB lower than with reference ref716 on the xz plane. On the yz plane, the CNR of ref716 is 2.9, 1.7,

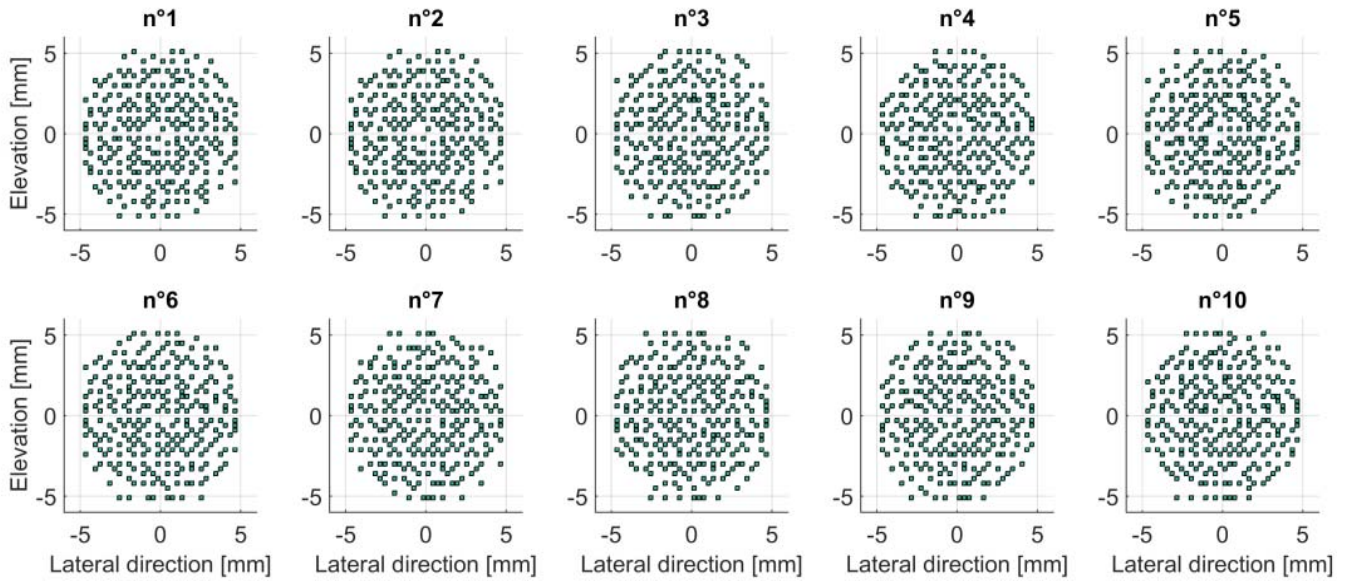


Fig. 12. Final layouts of the ten optimized arrays with identical optimization setup but different initial state S_0 .

TABLE IV
ENERGY FUNCTION VALUES ASSOCIATED WITH THE TEN ARRAYS OBTAINED USING AN IDENTICAL OPTIMIZATION SETUP BUT WITH DIFFERENT INITIAL STATES

Clone	n°1	n°2	n°3	n°4	n°5	n°6	n°7	n°8	n°9	n°10
$U (\times 10^6)$	111.5	111.5	108.2	113.7	113.9	110.3	109.5	111.1	108.3	111.4

and 1.0 dB higher than with opti128, opti192, and opti256, respectively. It can be noticed from Table III that the resolution and contrast performance on the yz plane are slightly better than on the xz plane (see discussion in Section V-D).

E. Design Robustness

The ten “clone” optimizations raised very similar results as it can be inferred from: Fig. 12, where the final layouts are shown; Table IV, which presents their associated energy value; and Fig. 13, where the radiated BP are presented in both the steered and not steered cases. Qualitatively, the layouts shown in Fig. 12 present a striking similarity in the element distribution over the aperture. The associated energy function values are also very close with mean and standard deviation 111 ± 2 . However, the energy value is not a sufficient comparison criterion. For example, the comparison between opti256 and ref716 (Section IV-A) has shown that for close energy function values the solutions can yield substantially different performance (see discussion in Section V-B). Hence, to highlight the acoustic performance robustness of the ten clones, their associated radiated BP are displayed in Fig. 13. Analyzing the BP of the ten clones, the mean and standard deviation of the SLL is -24.1 ± 0.6 dB, -24.6 ± 1.4 dB, and -23.7 ± 1.4 dB at depths R_1 , R_2 , and R_3 .

The acoustic performance improvement is highlighted in Fig. 13, when comparing both the not steered (top) and steered cases the BP of the ten initial random arrays (red dotted lines) and the optimized clones (blue solid lines). The SLL reduction is about 10 dB in both the steered and not steered

cases at focal depth 40 mm and it can reach more than 12 dB at depths 30 and 50 mm. The resolution at -6 dB is 0.5° coarser for the optimized clones.

V. DISCUSSION

A. Generalities

The general purpose of this paper was essentially to present, step-by-step, a method combining stochastic optimization and wideband acoustic simulation to design and evaluate 2-D ultrasonic sparse arrays. The practical case study illustrates how specific constraints raised by the targeted application and the fabrication process can be taken into account in the optimization design. In particular, it is shown how the method can be adapted to the number of independent channels on the available imaging system. The guidelines to define the energy function were also illustrated by the case study in order to easily identify the main challenging specifications that will shape the BP. The presented results aimed at illustrating the link between the layout geometry, the resulting BP (several depths and in 3-D), and the imaging capability in terms of resolution and contrast.

B. About the Multidepth Energy Function and the Layouts

First of all, it can be noticed in Fig. 6 (top) that the ML of the optimized arrays fits under the MASK, especially at depth 50 mm (Table II). This is assessed quantitatively from Table II where all the optimized arrays present an ML width at -20 dB, which is at least (considering the worst case of opti128) 0.4° (R_1), 1.4° (R_2), and 3.8° (R_3) narrower

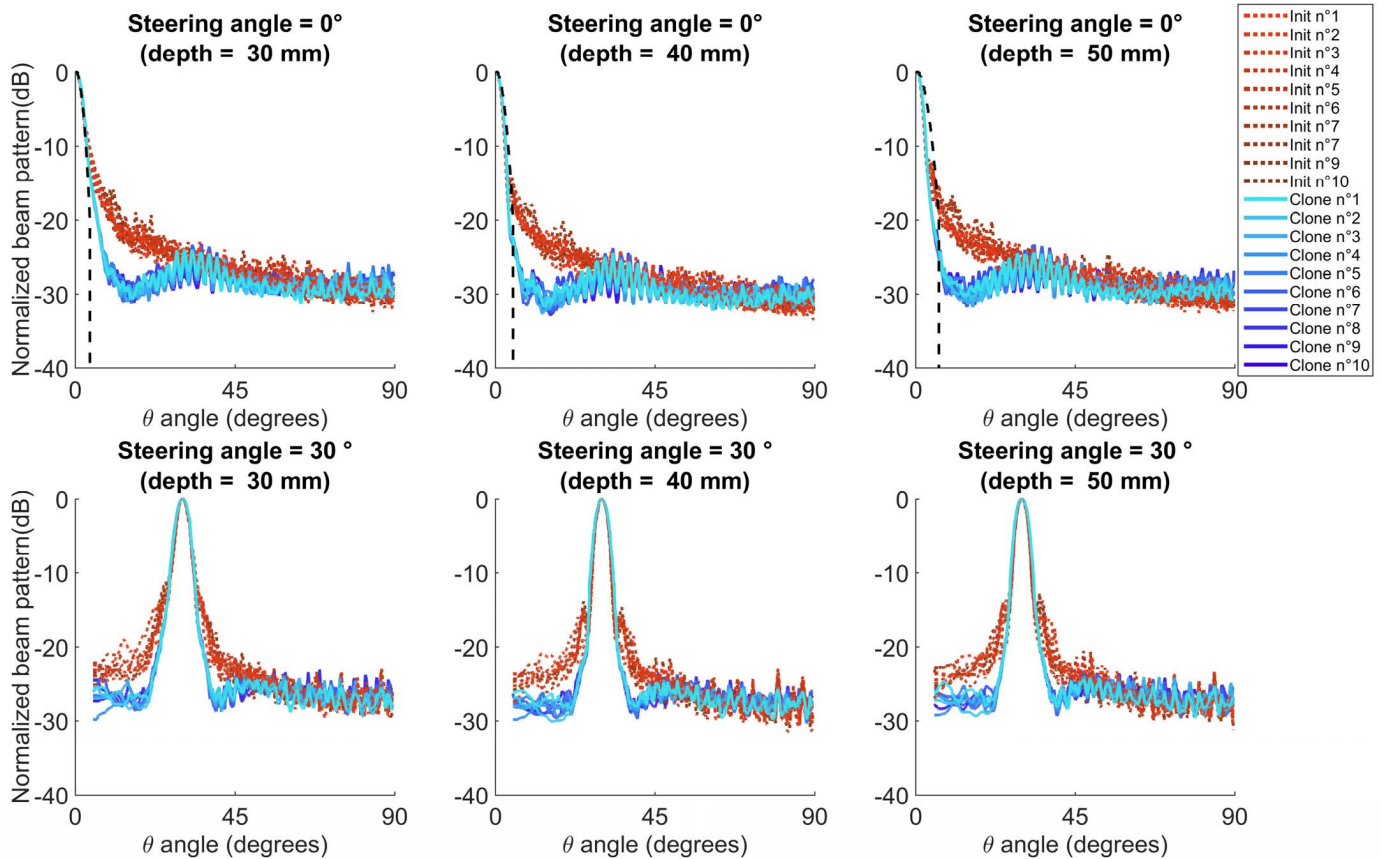


Fig. 13. Radiated BPs (worst case) at depths 30 (left), 40 (center), and 50 mm (right) of the ten optimization clones. The constraints MASK is shown as dotted lines. The steering angles were 0° (top panels) and 30° (bottom panels).

than the MASK constraint (see Section II-A3). A broader ML at 50 mm would further reduce the SLL, but this would be valuable only if, at the same time, the MASK was still respected at the other depths. The energy function definition implies that if the resolution constraint is respected, i.e., if the ML fits under the sculpting function $f(R, \theta)$, then the optimization continues pushing down the SLL (and indirectly the flat *plateau*) as low as possible. As in [35], [37], and [40], there is no *a priori* on the minimum GLL and SLL values that must be reached, i.e., the goal is the lowest achievable value for $M(R)$. This may explain why, with similar resolution performance, the optimized arrays that yield the lowest values of energy function are those of the lowest SLL.

However, as mentioned in Section IV-A, the reference array ref1024 that has the best results in terms of imaging capability (see Sections IV-C and IV-D), is not associated with the lowest value of U^{Nh} . This exception of ref1024 can be explained looking at the high sidelobes close to its ML (-19.5 , -16.6 , and -13.7 dB at respective depths R_1 , R_2 , and R_3), which inevitably penalizes the ref1024 configuration. However, $U^{Nh}(\text{ref1024})$ does not yield the highest energy function value because the penalty induced by the high SLL is compensated by a low energy ratio ($P_{\text{out}}/P_{\text{in}}$) that can be inferred from the very low SLL_{ave} value compared to the optimized arrays. The high SLL of ref1024 can be reduced using an apodization window, for instance the SLL values are

-19.6 dB (R_1), -20.3 dB (R_2), and -21.6 dB (R_3) with a 2-D Hanning apodization window on ref1024. This is in average 11 dB higher compared to the SLL yielded by the same apodized 32×32 element array but without deactivated lines. It appears that the three deactivated lines are also responsible for the high SLL. These remarks are also valid for ref716 and the high SLL that are visible along the y -axis in Figs. 7 and 8 are also caused by the three deactivated lines. It is noteworthy that integrating the fabrication constraints in the optimization process yielded SLL of the optimized arrays that are lower than with the apodized ref1024 array: it seems that the effect of the three deactivated lines is attenuated by the optimized aperiodic organization of the active elements.

This highlights how crucial the energy function definition is. Although ref1024 is not associated with the lowest energy value, it outperforms the optimized arrays in terms of imaging capabilities (1024 elements are expected to perform better than a quarter of them). This limitation means that solutions with better imaging capabilities may be avoided because the proposed energy function penalizes a high SLL (peak) without considering the SLL_{ave} . However, a quality of the obtained optimized solutions is that the SLL is lower than with ref716 and ref1024, and this at all of the three considered depths. From this point of view, the target of the proposed energy function is achieved but it requires further refinements (Section V-F1) to match with the best imaging performance.

In the proposed method, the deactivation of the corner elements was spontaneous, and therefore it might be inferred from the chosen energy function. This function was in fact defined to fit a beam shape with circular symmetry, which is a typical feature of circular apertures.

C. About the 3-D Beam Pattern Simulations

From Fig. 9, it can be seen that the median SLL decreases when the number of active elements increases, but it can also be noticed that the range of variation of the SLL is higher with ref1024. As a general trend for the evaluated 3-D metrics, a small range of variation should be preferred to guarantee homogeneous imaging capability over the entire volume. The smaller the range of variation, the less the image appearance depends on the steering angle, which is desired in practice. As announced in Section III-A2 for the circular aperture ref716, the confinement of the elements in a disk shape, significantly reduces the range of variation of the SLL compared to ref1024. Moreover, it can be noticed that it impacts on the SLL: the highest SLL encountered with ref716 over the 81 steering angles is 2 dB lower than with ref1024. The trend of reducing the SLL using a circular aperture is also reported in Table II where the values at depth R_1 (-1.7 dB with ref716 rather than ref1024) are consistent with the 3-D simulations and where the SLL reduction is stronger at depth R_2 (-4.6 dB) and R_3 (-8.7 dB). The lateral resolution performance (Fig. 9) appears to be very similar to the three optimized arrays. This is mainly due to the MASK that sculpted the same ML shape for all the optimized arrays (Fig. 6). A low SMER value indicates that the acoustic energy is concentrated inside the -6 dB isosurface, i.e., the remaining amount of pressure that could create the lateral artifacts is reduced. The sensitivity indicates the highest pressure value generated by the array (generally at focal point) normalized on the maximum of pressure obtained with ref1024. The sensitivity performance is directly impacted by the number of active elements, and Fig. 9 confirms that the sensitivity increases to ~ 6 dB when the number of elements, i.e., the active surface, is doubled (Fig. 9).

For all the optimized arrays, the ranges of variation of lateral resolution (0.3 mm), DOF (8 mm), SMER (3.2 dB), and sensitivity (1 dB) are very close to those obtained with ref716. The range of variation of the SLL (3.5 dB) is divided by four with the optimized arrays compared to that obtained with ref1024. The relatively small variation range obtained on the 3-D field metrics with the optimized arrays is positively surprising since only one steering angle at $(\theta, \phi) = (0^\circ, 0^\circ)$ is considered during the optimization process. The optimized layouts yield a similar behavior for all of the steering directions, thanks to its circular symmetry. Again, such symmetry may be associated with the chosen energy function, which imposes the minimization of the lateral lobes, at three depths, for all the ϕ angles (see Section V-B).

The comparison over all the 3-D metrics in Fig. 9 shows that opti192 and opti256 perform almost identically and it is also verified on the 3-D volume images that were simulated.

D. About the 3-D Volume Images

The resolution images (Fig. 10) and Table III show the optimized array yield resolution performance that is very close (2.4/2.1 mm average in xz/yz planes). This may be a consequence of using the same MASK to sculpt the ML shape. The resolution yielded by ref716 is 35% (xz plane) and 64% (yz plane) coarser compared to ref1024: the trade of switching off the corner elements is an increase in the lateral resolution because it reduces the dimensions of the active aperture (see Table III). The key point here is the contrast images (Fig. 11), where opti192 yields almost the same results as opti256. From Table III, compared to opti128 it can be noticed that opti192 and opti256 improve the CNR of 1.7 dB (xz plane) / 1.7 dB (yz plane) and 1.7 dB (xz plane)/1.9 dB (yz plane), respectively. This highlights a relationship between the imaging contrast capability of the optimized array and the level of their BP *plateau* (Fig. 6) described in Section IV-B: the *plateau* of opti192 and opti256 are both ~ 2 dB below the *plateau* of opti128.

Moreover, the fact that better images are obtained on the yz rather than on the xz plane can be explained by the rectangular geometry of the footprint caused by the three inactive lines. Indeed, the aperture dimension of ref1024 on the x -axis (9.6 mm) is slightly narrower than on the y -axis (10.5 mm). The same trend can be observed on the optimized layouts: a wider aperture dimension along the y -axis provides better imaging capabilities in a plane containing this same direction. On the contrary, in Table III the resolution performance raised by ref716 is the same in both the xz and yz planes because it has the same aperture dimension along the x - and y -axes.

E. About the Design Robustness

The design robustness was analyzed through the optimization of ten “clones” as described in Section III-E3. It can be seen from Fig. 13 that the obtained BP are robust with the initial state. The comparison with the initial states clearly shows the improvement yielded by the optimization on the radiated BP, and this at the three depths R_1 , R_2 , and R_3 . The resolution at -6 dB presented in Table II suggests that for all the optimized arrays, the resolution constraint was not strong enough to reach the performance of the reference arrays ref716 and ref1024. Hence, a new MASK definition (see Section III-E3) was tested to improve the resolution performance. Unfortunately, compared to opti256 the SLL is 2.5 dB (R_1), 2.3 dB (R_2), and 2.9 dB (R_3) higher with the clones (mean over the ten clones), which may be due to a too strong resolution constraint at depth R_1 . Indeed, it can be noticed in Fig. 13 that at depth $R_1 = 30$ mm the ML goes beyond the MASK, whereas at depth $R_3 = 50$ mm there is a little space between the ML and the MASK. To some extent, the resolution improvement was achieved since the mean -6 dB resolution for the clones is, respectively, 92%, 95%, and 86% than that of opti256. Hence the energy function should be carefully defined, taking into consideration that it is not possible to reach a resolution as thin as desired without a strong increase in the SLL.

F. Perspectives

1) *About the Energy Function:* As discussed in Section V-B, the energy function may be improved by mixing the minimization of the SLL with the minimization of the SLL_{ave} , which may enable a higher SLL while lowering the SLL_{ave} values.

As mentioned in Section V-C, a homogeneous imaging capability over the entire volume is desired to avoid any dependencies between the image quality and the orientation of the probe handle. In this paper, a relatively good homogeneity of the acoustic properties is obtained (see Section IV-C) over a 3-D sector of -32° , $+32^\circ$ with only one steering angle ($\theta = 0^\circ$, $\phi = 0^\circ$) considered in the optimization. However, one could think about integrating in the energy function the steering capability of the array. This could be implemented by simulating the BP for N_{steer} angles of steering at each step of the optimization, but the optimization would last N_{steer} times longer because of the required additional simulation.

As mentioned in Section II-A3, a different weighting for the different hemispheres can be implemented to give priority to the performance at a particular depth. One could add more hemispheres, or also investigate the impact of an energy function directly defined on the 3-D BP of an array. However, for an effective sculpting of the 3-D BP, the PMPs should be located in the entire 3-D volume above the array (not only at three depths). It would require a lot more computation power, demanding GPU implementation, to define an energy function based on the emitted 3-D BP in the volume.

2) *About the State Space and Acoustic Simulation:* The state-space definition depends on the parameters that can be taken into account by the acoustic simulator. Currently, the following degrees of freedom are available and their impact on the image quality will be investigated in the future work: out-of-grid (free) positioning of the elements, element size and orientation, excitation signal, and individual impulse response of the elements. An extension to a more complex model of the array of transducers (especially to consider the electrical and acoustic interface, i.e., the materials involved in the transduction) would be possible using a Multiphysics simulator but it may require a specific implementation and more computation power. A possibility to be more realistic with the presented work would be to physically measure the individual impulse response of all the 1024 elements of ref1024 and integrate them in the acoustic simulation used for the optimization. This could penalize the elements with a very bad quality response—dead elements—and prevent from connecting them in the optimal array. Following the same idea, the state space could be restricted to the elements that show a satisfying impulse response, which means to withdraw any defective element from the possible candidates.

In this paper, the same array is used for both TX and RX of the US waves aiming at maximizing the array sensitivity. However, one could think about modifying the state space to optimize the combination of two arrays, one with N_{TX} elements in TX and another with N_{RX} elements in RX as in [28], [29], [33], [35], and [37]. The number of elements of each array could be part of the optimization with for instance $N_{TX} + N_{RX} = 256$ if 256 independent channels are available.

In this case, however, the presented multidepth energy function sculpting the ML shape would be adapted to the two-way (pulse-echo) BP and not to the one-way BP.

VI. CONCLUSION

The optimization of 2-D sparse arrays for 3-D US imaging has been addressed using an SA algorithm. An innovative control of the 3-D acoustic behavior was achieved thanks to a multidepth energy function that sculpts the BP at multiple depths. The proposed approach was illustrated with an example of 2-D sparse optimization where the aim was to find the best selection of 128, 192, and 256 active elements within a 3 MHz 32×32 gridded 2-D array. The 1024-element 2-D array and the 716-element circular array, obtained after corner deactivation, were both considered as references. The obtained layout geometries were compared in terms of SLL and resolution on the radiated BP at depths of 30, 40 (focal depth), and 50 mm. Additional 3-D BP simulations with 81 steering angles for each array were performed to evaluate the performance homogeneity over a wide range of steering angles. Finally, both resolution and contrast phantoms were simulated to quantify the 3-D imaging capabilities of the arrays.

The possible fabrication constraints can be finally taken into account before starting the design of the transducer. Additionally, the integration of wideband acoustic simulations inside the optimization process will enable new degrees of freedom such as the arbitrary positioning of the elements, the orientation of the elements, or the excitation signal.

REFERENCES

- [1] R. W. Prager, U. Z. Ijaz, A. H. Gee, and G. M. Treece, "Three-dimensional ultrasound imaging," *Proc. Inst. Mech. Eng. H, J. Eng. Med.*, vol. 224, no. 2, pp. 193–223, Feb. 2010.
- [2] G. D. Stetten *et al.*, "Real-time 3D ultrasound: A new look at the heart," *J. Cardiovascular Diagnosis Procedures*, vol. 15, no. 2, pp. 73–84, 1998.
- [3] J.-F. Deprez, E. Brusseau, C. Schmitt, G. Cloutier, and O. Basset, "3D estimation of soft biological tissue deformation from radio-frequency ultrasound volume acquisitions," *Med. Image Anal.*, vol. 13, no. 1, pp. 116–127, Feb. 2009.
- [4] T. Deffieux, J. L. Gennisson, M. Tanter, and M. Fink, "Assessment of the mechanical properties of the musculoskeletal system using 2-D and 3-D very high frame rate ultrasound," *IEEE Trans. Ultrason., Ferroelect., Freq. Control*, vol. 55, no. 10, pp. 2177–2190, Oct. 2008.
- [5] B. Y. S. Yiu, S. S. M. Lai, and A. C. H. Yu, "Vector projectile imaging: Time-resolved dynamic visualization of complex flow patterns," *Ultrasound Med. Biol.*, vol. 40, no. 9, pp. 2295–2309, Sep. 2014.
- [6] Y. Zhao, A. Bernard, C. Cachard, and H. Liebgott, "Biopsy needle localization and tracking using ROI-RK method," *Abstract Appl. Anal.*, vol. 2014, Oct. 2014, Art. no. 973147.
- [7] C. Nadeau, H. Ren, A. Krupa, and P. Dupont, "Intensity-based visual servoing for instrument and tissue tracking in 3D ultrasound volumes," *IEEE Trans. Autom. Sci. Eng.*, vol. 12, no. 1, pp. 367–371, Jan. 2015.
- [8] G. Unsgaard *et al.*, "Intra-operative 3D ultrasound in neurosurgery," *Acta Neurochirurgica*, vol. 148, no. 3, pp. 235–253, Mar. 2006.
- [9] F. Lindseth *et al.*, "Ultrasound-based guidance and therapy," in *Advancements and Breakthroughs in Ultrasound Imaging*. Rijeka, Croatia: InTech, 2013, pp. 28–82.
- [10] E. D. Light, S. F. Idriss, P. D. Wolf, and S. W. Smith, "Real-time three-dimensional intracardiac echocardiography," *Ultrasound Med. Biol.*, vol. 27, no. 9, pp. 1177–1183, Sep. 2001.
- [11] L. Sugeng *et al.*, "Quantitative assessment of left ventricular size and function: Side-by-side comparison of real-time three-dimensional echocardiography and computed tomography with magnetic resonance reference," *Circulation*, vol. 114, no. 7, pp. 654–661, Aug. 2006.

- [12] O. T. V. Ramm and S. W. Smith, "Beam steering with linear arrays," *IEEE Trans. Biomed. Eng.*, vol. BME-30, no. 8, pp. 438–452, Aug. 1983.
- [13] M. F. Rasmussen, T. L. Christiansen, E. V. Thomsen, and J. A. Jensen, "3-D imaging using row-column-addressed arrays with integrated apodization—Part I: Apodization design and line element beamforming," *IEEE Trans. Ultrason., Ferroelect., Freq. Control*, vol. 62, no. 5, pp. 947–958, May 2015.
- [14] T. L. Christiansen, M. F. Rasmussen, J. P. Bagge, L. N. Moesner, J. A. Jensen, and E. V. Thomsen, "3-D imaging using row-column-addressed arrays with integrated apodization—Part II: Transducer fabrication and experimental results," *IEEE Trans. Ultrason., Ferroelect., Freq. Control*, vol. 62, no. 5, pp. 959–971, May 2015.
- [15] J. Provost *et al.*, "3D ultrafast ultrasound imaging *in vivo*," *Phys. Med. Biol.*, vol. 59, no. 19, p. L1, Oct. 2014.
- [16] J. Kortbek, J. A. Jensen, and K. L. Gammelmark, "Sequential beamforming for synthetic aperture imaging," *Ultrasonics*, vol. 53, no. 1, pp. 1–16, Jan. 2013.
- [17] G. Matrone, A. S. Savoia, M. Terenzi, G. Caliano, F. Quaglia, and G. Magenes, "A volumetric CMUT-based ultrasound imaging system simulator with integrated reception and μ -beamforming electronics models," *IEEE Trans. Ultrason., Ferroelect., Freq. Control*, vol. 61, no. 5, pp. 792–804, May 2014.
- [18] R. Fisher *et al.*, "Reconfigurable arrays for portable ultrasound," in *Proc. IEEE Ultrason. Symp.*, vol. 1. Sep. 2005, pp. 495–499.
- [19] I. O. Wygant *et al.*, "An integrated circuit with transmit beamforming flip-chip bonded to a 2-D CMUT array for 3-D ultrasound imaging," *IEEE Trans. Ultrason., Ferroelect., Freq. Control*, vol. 56, no. 10, pp. 2145–2156, Oct. 2009.
- [20] K. Chen, "A column-row-parallel ASIC architecture for 3D wearable/portable medical ultrasonic imaging," Ph.D. dissertation, Dept. Elect. Eng. Comput., Massachusetts Inst. Technol., Cambridge, MA, USA, 2014.
- [21] A. S. Logan, L. L. P. Wong, A. I. H. Chen, and J. T. W. Yeow, "A 32×32 element row-column addressed capacitive micromachined ultrasonic transducer," *IEEE Trans. Ultrason., Ferroelect., Freq. Control*, vol. 58, no. 6, pp. 1266–1271, Jun. 2011.
- [22] B. Savord and R. Solomon, "Fully sampled matrix transducer for real time 3D ultrasonic imaging," in *Proc. IEEE Symp. Ultrason.*, vol. 1. Oct. 2003, pp. 945–953.
- [23] O. T. von Ramm and S. W. Smith, "Three-dimensional imaging system," U.S. Patent 4694434 A, Sep. 15, 1987.
- [24] S. Holm, A. Austeng, K. Iranpour, and J.-F. Hopperstad, "Sparse sampling in array processing," in *Nonuniform Sampling*, F. Marvasti, Ed. New York, NY, USA: Springer, 2001, pp. 787–833.
- [25] A. Ramalli, E. Boni, A. S. Savoia, and P. Tortoli, "Density-tapered spiral arrays for ultrasound 3-D imaging," *IEEE Trans. Ultrason., Ferroelect., Freq. Control*, vol. 62, no. 8, pp. 1580–1588, Aug. 2015.
- [26] S. Ramadas, J. Jackson, J. Dziewierz, R. O'Leary, and A. Gachagan, "Application of conformal map theory for design of 2-D ultrasonic array structure for NDT imaging application: A feasibility study," *IEEE Trans. Ultrason., Ferroelect., Freq. Control*, vol. 61, no. 3, pp. 496–504, Mar. 2014.
- [27] O. Martínez-Graullera, C. J. Martín, G. Godoy, and L. G. Ullate, "2D array design based on Fermat spiral for ultrasound imaging," *Ultrasonics*, vol. 50, no. 2, pp. 280–289, Feb. 2010.
- [28] A. Austeng and S. Holm, "Sparse 2-D arrays for 3-D phased array imaging—Design methods," *IEEE Trans. Ultrason., Ferroelect., Freq. Control*, vol. 49, no. 8, pp. 1073–1086, Aug. 2002.
- [29] S. S. Brunke and G. R. Lockwood, "Broad-bandwidth radiation patterns of sparse two-dimensional vernier arrays," *IEEE Trans. Ultrason., Ferroelect., Freq. Control*, vol. 44, no. 5, pp. 1101–1109, Sep. 1997.
- [30] R. E. Davidsen, J. A. Jensen, and S. W. Smith, "Two-dimensional random arrays for real time volumetric imaging," *Ultrason. Imag.*, vol. 16, no. 3, pp. 143–163, Jul. 1994.
- [31] S. W. Smith, H. G. Pavy, and O. T. von Ramm, "High-speed ultrasound volumetric imaging system. I. Transducer design and beam steering," *IEEE Trans. Ultrason., Ferroelect., Freq. Control*, vol. 38, no. 2, pp. 100–108, Mar. 1991.
- [32] D. H. Turnbull and F. S. Foster, "Beam steering with pulsed two-dimensional transducer arrays," *IEEE Trans. Ultrason., Ferroelect., Freq. Control*, vol. 38, no. 4, pp. 320–333, Jul. 1991.
- [33] C. Sciallero and A. Trucco, "Design of a sparse planar array for optimized 3D medical ultrasound imaging," presented at the 23rd Eur. Signal Process. Conf. (EUSIPCO), Nice, France, Aug./Sep. 2015, pp. 1341–1345.
- [34] B. Diarra, M. Robini, P. Tortoli, C. Cachard, and H. Liebgott, "Design of optimal 2-D nongrid sparse arrays for medical ultrasound," *IEEE Trans. Biomed. Eng.*, vol. 60, no. 11, pp. 3093–3102, Nov. 2013.
- [35] C. Tekes, M. Karaman, and F. L. Degertekin, "Optimizing circular ring arrays for forward-looking IVUS imaging," *IEEE Trans. Ultrason., Ferroelect., Freq. Control*, vol. 58, no. 12, pp. 2596–2607, Dec. 2011.
- [36] P. Chen, B.-J. Shen, L.-S. Zhou, and Y.-W. Chen, "Optimized simulated annealing algorithm for thinning and weighting large planar arrays," *J. Zhejiang Univ. Sci. C*, vol. 11, no. 4, pp. 261–269, Apr. 2010.
- [37] J. W. Choe, Ö. Oralkan, and P. T. Khuri-Yakub, "Design optimization for a 2-D sparse transducer array for 3-D ultrasound imaging," in *Proc. IEEE Ultrason. Symp. (IUS)*, Oct. 2010, pp. 1928–1931.
- [38] A. Trucco, "Thinning and weighting of large planar arrays by simulated annealing," *IEEE Trans. Ultrason., Ferroelect., Freq. Control*, vol. 46, no. 2, pp. 347–355, Mar. 1999.
- [39] A. Austeng, S. Holm, P. K. Weber, N. Aakvaag, and K. Iranpour, "1D and 2D algorithmically optimized sparse arrays," in *Proc. IEEE Ultrason. Symp.*, vol. 2. Oct. 1997, pp. 1683–1686.
- [40] S. Holm and B. Elgetun, "Optimization of the beampattern of 2D sparse arrays by weighting," in *Proc. IEEE Ultrason. Symp.*, vol. 2. Nov. 1995, pp. 1345–1348.
- [41] P. K. Weber, R. M. Schmitt, B. D. Tylkowski, and J. Steck, "Optimization of random sparse 2-D transducer arrays for 3-D electronic beam steering and focusing," in *Proc. IEEE Ultrason. Symp.*, vol. 3. Oct./Nov. 1994, pp. 1503–1506.
- [42] R. L. Haupt, "Thinned arrays using genetic algorithms," *IEEE Trans. Antennas Propag.*, vol. 42, no. 7, pp. 993–999, Jul. 1994.
- [43] S.-F. Hwang and R.-S. He, "Improving real-parameter genetic algorithm with simulated annealing for engineering problems," *Adv. Eng. Softw.*, vol. 37, no. 6, pp. 406–418, Jun. 2006.
- [44] D. Adler, "Genetic algorithms and simulated annealing: A marriage proposal," in *Proc. IEEE Int. Conf. Neural Netw.*, vol. 2. Mar./Apr. 1993, pp. 1104–1109.
- [45] E. Roux, B. Diarra, M. Robini, C. Cachard, P. Tortoli, and H. Liebgott, "Realistic acoustic simulation of 2-D probe elements in simulated annealing sparse array optimization," in *Proc. IEEE Int. Ultrason. Symp. (IUS)*, Sep. 2014, pp. 2125–2128.
- [46] B. Diarra *et al.*, "Optimization of free-moving elements in 2D ultrasound sparse arrays," in *Proc. IEEE Int. Ultrason. Symp. (IUS)*, Sep. 2014, pp. 2189–2192.
- [47] E. Roux, A. Ramalli, P. Tortoli, C. Cachard, M. Robini, and H. Liebgott, "Speed-up of acoustic simulation techniques for 2D sparse array optimization by simulated annealing," in *Proc. IEEE Int. Ultrason. Symp. (IUS)*, Oct. 2015, pp. 1–4.
- [48] E. Roux, A. Ramalli, M. Robini, H. Liebgott, C. Cachard, and P. Tortoli, "Spiral array inspired multi-depth cost function for 2D sparse array optimization," in *Proc. IEEE Int. Ultrason. Symp. (IUS)*, Oct. 2015, pp. 1–4.
- [49] A. Ramalli and P. Tortoli, "256-element density-tapered spiral matrices for ultrasound phased imaging," in *Proc. IEEE Int. Ultrason. Symp. (IUS)*, Sep. 2014, pp. 2087–2090.
- [50] A. S. Savoia, G. Caliano, and M. Pappalardo, "A CMUT probe for medical ultrasonography: From microfabrication to system integration," *IEEE Trans. Ultrason., Ferroelect., Freq. Control*, vol. 59, no. 6, pp. 1127–1138, Jun. 2012.
- [51] S. Kirkpatrick, C. D. Gelatt, and M. P. Vecchi, "Optimization by simulated annealing," *Science*, vol. 220, no. 4598, pp. 671–680, 1983.
- [52] P. J. M. van Laarhoven and E. H. L. Aarts, *Simulated Annealing*. Dordrecht, The Netherlands: Springer, 1987.
- [53] M. C. Robini, "Theoretically grounded acceleration techniques for simulated annealing," in *Handbook of Optimization*, I. Zelinka, V. Snášel, and A. Abraham, Eds. Berlin, Germany: Springer, 2013, pp. 311–335.
- [54] M. C. Robini and P.-J. Reissman, "From simulated annealing to stochastic continuation: A new trend in combinatorial optimization," *J. Global Optim.*, vol. 56, no. 1, pp. 185–215, May 2013.
- [55] S. Barnes, M. Bolorforosh, and R. Phelps, "System and method for 2D partial beamforming arrays with configurable sub-array elements," U.S. Patent 2005 0228277 A1, Oct. 13, 2005.
- [56] K. E. Thomenius, R. G. Wodnicki, and Y.-M. Li, "Transmit and receive interface array for highly integrated ultrasound scanner," U.S. Patent 7775979 B2, Aug. 17, 2010.
- [57] J. A. Jensen, "Field: A program for simulating ultrasound systems," *Med. Biol. Eng. Comput.*, vol. 34, no. 1, pp. 351–353, 1996.

- [58] J. A. Jensen and N. B. Svendsen, "Calculation of pressure fields from arbitrarily shaped, apodized, and excited ultrasound transducers," *IEEE Trans. Ultrason., Ferroelect., Freq. Control*, vol. 39, no. 2, pp. 262–267, Mar. 1992.
- [59] A. H. Nuttall, "Some windows with very good sidelobe behavior," *IEEE Trans. Acoust., Speech, Signal Process.*, vol. 29, no. 1, pp. 84–91, Feb. 1981.



Emmanuel Roux (S'14) was born in Firminy, France, in 1990. He received the M.Sc. degree in electrical and electronics engineering and the M.Sc. degree in science for technologies and health from the Lyon National Institute of Applied Sciences (INSA-Lyon) in 2013. He is currently pursuing the Ph.D. degree in acoustics and information engineering with the University of Lyon, Lyon, France, and the University of Florence, Florence, Italy.

He teaches applied mathematics at the Electrical Engineering Department, Technical Institute of Université Claude Bernard Lyon 1, Villeurbanne, France. His current research interests include 2-D transducer optimization for 3-D ultrasound imaging and is particularly interested in 3-D acoustics, stochastic optimization, and information processing for health and entertainment sectors.



Alessandro Ramalli (S'10–M'12) was born in Prato, Italy, in 1983. He received the bachelor's degree in electronics engineering and the Ph.D. degree in electronics system engineering from the University of Florence, Florence, Italy, in 2008. In 2012, he earned the Ph.D. degree in automatics, systems, and images from the University of Lyon, Lyon, France, by defending a thesis on the development of novel ultrasound techniques for imaging and elastography.

He currently holds a postdoctoral position with the MSD Laboratory, University of Florence, where he is involved in the development of the imaging section of a programmable open ultrasound system. His current research interests include medical imaging, ultrasound simulation, and elastography.



Hervé Liebgott (S'03–A'05) was born in France in 1979. He received the Ph.D. degree from Lyon National Institute of Applied Sciences, Lyon, France, in 2005 and the French Habilitation (Hdr) degree from University Lyon 1, Lyon, in 2011.

He is an Associate Professor with the Department of Electrical Engineering, University Institute of Technology Lyon 1, IUT Lyon 1 (GEII), Villeurbanne, France, and is doing his research at the CREATIS Laboratory, INSA-Lyon, Université de Lyon, Lyon, where he is currently the Vice Leader of the ultrasound imaging team. His current research interests include image and signal processing applied to medical ultrasound imaging and is particularly interested in image formation techniques and motion estimation.

Dr. Liebgott has been a Junior Member of the French Institut Universitaire de France since 2014. He has been an Associate Member of the IEEE Bio Imaging and Signal Processing Technical Committee and a member of the IEEE International Ultrasonics Symposium Technical Program Committee, since 2014. He has been an Associate Editor of IEEE TRANSACTIONS ON ULTRASONICS, FERROELECTRICS, AND FREQUENCY CONTROL, since 2015.



Christian Cachard received the Ph.D. degree in acoustics, with a specialization in signal processing for underwater acoustics from INSA-Lyon, Lyon, France, in 1988.

He joined the research laboratory at CREATIS, INSA-Lyon, Université de Lyon, Lyon, and his research interests included ultrasound medical imaging, ultrasound contrast agent imaging, ultrasound radio frequency processing, microtools localization in 3-D ultrasound data, and 2-D matrix arrays for 3-D imaging. He is currently a Professor with the Electrical Engineering Department, Technical Institute of Université Claude Bernard Lyon 1, Villeurbanne, France. He is a coauthor for 38 papers in peer-reviewed journals and has supervised 18 Ph.D. students.



Marc C. Robini received the M.Sc. degree in electrical and computer engineering and the Ph.D. degree in signal and image processing from INSA-Lyon Engineering University, Lyon, France, in 1993 and 1998, respectively.

In 1999, he joined INSA-Lyon, where he is currently an Associate Professor of mathematics and a Research Associate with the Center for Research and Applications in Image and Signal Processing (CREATIS), CNRS Research Unit UMR5220, and INSERM Research Unit U1206, Villeurbanne, France. His current research interests include deterministic and stochastic optimization methods for large-scale inverse problems.



Piero Tortoli (M'91–SM'96) received the Laurea degree in electronics engineering from the University of Florence, Firenze, Italy, in 1978.

He has been a Faculty Member with the Electronics and Telecommunication (now Information Engineering) Department, University of Florence, where he is currently a Full Professor of Electronics, leading a group of over 10 researchers at the Microelectronics Systems Design Laboratory. His current research interests include the development of ultrasound research systems and novel imaging/Doppler methods, on which he has authored more than 200 papers.

Prof. Tortoli was named an Honorary Member of the Polish Academy of Sciences. He has been serving on the IEEE International Ultrasonics Symposium Technical Program Committee since 1999. He is currently an Associate Editor of IEEE TRANSACTIONS ON ULTRASONICS, FERROELECTRICS, AND FREQUENCY CONTROL. He chaired the 22nd International Symposium on Acoustical Imaging in 1995 and the 12th New England Doppler Conference in 2003, and established the Artimino Conference on Medical Ultrasound in 2011.